Faculté des sciences

Linking landslide dynamics with sediment transfer in the Swiss Alps

Case study on landslide-driven sediment dynamics in the Rhône Valley

Auteur :
Mathilde Bayens

Promoteurs :
François Clapuyt et Veerle Vanacker

Lecteur :
Bas van Wesemael

Année académique 2020-2021
Mémoire présenté en vue de l'obtention du grade académique de master en sciences géographiques, orientation générale

Remerciements

Je tiens à remercier sincèrement toutes les personnes qui m’ont permis d’aboutir à la rédaction de ce mémoire.

Dans un premier temps, je souhaite évidemment remercier mes promoteurs, François Clapuyt et Veerle Vanacker, pour leur disponibilité, leurs encouragements et leurs conseils avisés tout au long de ce travail.

Je remercie ensuite mes parents, Benoit et Nathalie, ainsi que toute ma famille, pour leur constant soutien et leurs encouragements dont j’ai grandement eu besoin tout au long de cette année si particulière.

Toute ma gratitude va également à Joonas, pour ses corrections et sa relecture.

Enfin, je remercie grandement mes amis géographes, et Louise, pour leur présence, leurs précieux conseils et encouragements qui m’ont permis d’aboutir à la réalisation de ce mémoire concluant cinq années d’étude en Sciences géographiques à l’UCLouvain.

Table of contents

Introduction 1

1. Literature Review 3
   - 1.1. Landscape evolution 3
   - 1.2. Hillslope processes in mountainous environments 4
   - 1.3. Sediment connectivity 5
   - 1.4. Methods to assess sediment budget in mountainous areas 6
     - 1.4.1. CRN dating method for long-term quantification 6
     - 1.4.2. Landslide mapping for short-term quantification 8
     - 1.4.3. Connectivity indices 12
   - 1.5. Research questions 13
2. Study area 15
3. Material and methods 17
   - 3.1. Compilation of landslide inventory 17
   - 3.2. Statistical analysis: magnitude-frequency distributions 18
   - 3.3. The estimated total volume of landslide material (and *LMR*) 19
   - 3.4. Connectivity index 19
4. Results 25
   - 4.1. Landslide inventory and frequency-area distribution 25
   - 4.2. Landslide mobilization rates (and denudation rates) 27
   - 4.3. Connectivity index (IC) 28
5. Discussion 33
   - 5.1. Landslide inventory and magnitude-frequency statistics 33
   - 5.2. Landslide mobilization rates 35
   - 5.3. Denudation rates 35
   - 5.4. Sediment connectivity indices 38
   - 5.5. Comparison and relation between the main results: magnitude-frequency distribution, denudation rate and sediment connectivity 41
6. Conclusion 43
7. References 45
8. List of figures 57
9. List of tables 59
10. Appendix 60

Introduction

Over time, the surface topography evolves in response to interactions and feedbacks between climate, erosion and tectonic processes. Erosion and weathering processes lead to surface denudation (Roe et al. 2008; Stanley et Luczaj 2015). Erosion processes such as landslides are a main driver of landscape evolution and a dominant source of sediments, especially in steep and mountainous regions (Vanacker et al. 2015). However, the role of landsliding in sediment mobilization and denudation remains poorly understood and quantified (Clapuyt et al. 2019; Broeckx et al. 2020). Based on empirical data of landslide inventories, the number of landslides that occur at different sizes can be quantified by frequency-area distribution.

Several studies have proposed that the frequency-area distribution of medium and large landslides follows a power law distribution (Hovius et al. 1997; Guzzetti et al. 2002; Malamud et al. 2004; Guzzetti et al. 2009; Larsen et al. 2010; Tanyaş et al. 2019). However, Guzzetti et al. (2002) and Malamud et al. (2004) reported a divergence of the frequency of small landslides from the power law distribution, and proposed alternative approaches based on the inverse-gamma distribution. Relying on the landslide frequency-area distribution, the average landslide mobilization rate (*LMR*) can be derived. The *LMR* value represents the volume of landslide-derived sediment that is displaced per unit of area per year [m^3 km^{-2} yr^{-1}] (Guzzetti et al. 2009; Vanacker et al. 2020), and provides insights on the geomorphological impact of landslides in sediment source areas (Broeckx et al. 2020).

By studying the transfer of landslide-derived sediment from the source areas to the fluvial system, it is possible to acquire observations on the long-term topographic evolution of landslide-affected areas. Bracken et al. (2015) proposed the framework of sediment connectivity to study the transfer of sediment from a source to a sink in a catchment, and the movement of sediment between different zones within a catchment. The sediment connectivity index (*IC*) developed by e.g. Borselli et al. (2008) allows the computation of the potential connections between hillslope sediment sources and the fluvial networks.

The evacuation of sediment by the fluvial network can be derived from in-situ produced cosmogenic nuclides, such as beryllium-10 (^{10}Be), in soils and sediments (Bierman et al. 2005; Binnie et al. 2007; Vanacker, von Blanckenburg, Hewawasam, et al. 2007). Norton et al. (2010) computed denudation rates over late Holocene timescales (0.5-3 kyr) in 13 catchments of the upper Rhône Valley in the Swiss Alps. They reported rates that varied by more than two orders of magnitude, and were dependent on the presence of glaciers in the headwater basins.

The objective of this work is to contribute to a better understanding of landslide-driven sediment dynamics in mountainous regions. More specifically, the following aspects were examined (i) the landslide distributions based on a new landslide inventory, (ii) the ratio of landslide mobilization rates to denudation rates and (iii) the spatial variation of sediment connectivity in alpine catchments was explored. This work is based on a case study of two catchments (one fluvial: *Nider* and one glacial: *Mins*) located in the upper Rhône Valley of the Swiss Alps.

This master's thesis is composed of five chapters. The first one is a literature review on landscape evolution, hillslope processes occurring in mountainous regions, sediment connectivity and methods to assess it. In the second chapter, the study area is presented with a geomorphological sketch of the upper Rhône Valley and the denudation rates of the two selected catchments. The third chapter is dedicated to data collection and processing: computation of the landslide inventory and magnitude-frequency distributions, estimation of *LMR* and *IC* values. The two final chapters present and discuss the results.

1. Literature Review

1.1. Landscape evolution

Over time and space, surface topography evolves in response to interactions and feedbacks between climate, erosion and tectonic processes. Climate influences erosion processes and climate is itself controlled by the topography. Erosion processes move mass within the system, while tectonic processes, e.g. convergence of lithospheric plates, add mass into it (Roe et al. 2008). Two components contribute to uplift: tectonic and isostatic components (Burbank et Anderson 2012). Rock uplift is the vertical motion of rocks relative to a reference level, i.e. usually the geoid (Stüwe et Barr 1998). Isostatic uplift, on the other hand, is the crustal rebound on the earth's mantle that isostatically compensates for the removal of materials by erosion (Bernet et al. 2001; Burbank et Anderson 2012; Mey et al. 2016).

In 1975, Hack proposed a landscape development model where landscapes come into a dynamic equilibrium when rates of deformation and rates of erosion are sustained for a long time period. A mountain range resulting from tectonic plate collision grows over time. At some point, the relief on hillslopes creates forces exceeding the rock strength leading to surface collapse. Even if rates of tectonic forcing persist for very long periods, the topography cannot indefinitely increase because of the limited strength of rocks. With continued bedrock uplift, additional slope failures will limit the height that the topography could attain. Eventually, the topography will reach a steady-state or a dynamic equilibrium (Hack 1975).

Denudation rates quantify the Earth's surface lowering per unit of time for a given spatial area (Burbank et Anderson 2012). Earth surface denudation occurs as a result of erosion and weathering processes. Weathering is a collective term for the chemical and physical processes that break down rocks of any kind. Physical weathering is the mechanical fragmentation of rock without chemical alteration, whereas chemical weathering is the alteration or dissolution of minerals in rocks (Gabet et Mudd 2009; Stanley et Luczaj 2015). Physical weathering is mainly controlled by ice, snow, water, temperature changes, as well as earth movements. When rock mass is exhumed, elastic strain release causes fractures and discontinuities in rocks which eventually exfoliate at the surface, ready to be subsequently weathered and eroded by external agents. In cold environments, frost shattering occurs due to temperature variations. Indeed, water expands when it freezes and the increase of pressure splits the rocks into smaller fractions of different sizes (Stanley et Luczaj 2015). Erosion is the process that mobilizes rock and sediment material at the surface and moves them downslope and downstream. Sediment is all material deposited on Earth’s surface by water, ice, or air, or by gravitational transport down a slope. Grains of sediment accumulate in a variety of sediment sinks such as landslide deposits, alluvial fans, river channels, lake bottoms, sandy beaches, and eventually seafloors (Stanley et Luczaj 2015). The type and magnitude of erosion and weathering processes depend on local conditions, i.e. climate, substrate, topography and tectonics (Aalto et al. 2006; Binnie et al. 2007; Turowski et Cook 2017). From the Middle Pleistocene (781 to 126 kyr) to the Pleistocene-Holocene boundary (11.7 kyr before the year

2000), the succession of glacial and non-glacial periods led to erosion processes and prevented landscapes to reach an equilibrium state (Burbank et al. 2012). At the global scale, Quaternary glaciations have eroded wide and over-steepened valleys (Peizhen et al. 2001).

1.2. Hillslope processes in mountainous environments

Over different spatial and temporal scales, tectonic and geomorphic processes are the main drivers of landscape evolution. In mountainous environments, river incision controls the evolution of surface topography by oversteepening hillslopes (Egholm et al. 2013; Vanacker et al. 2015). Steep slopes in turn adjust their morphometry with gully retreat, bank erosion and landslides (Fryirs 2013), whereas soil creep processes denude surrounding low-gradient slopes (Norton et al. 2010). Hillslope erosion mobilizes soil and regolith that can later be transported by gravity and water to the river network and subsequently further downstream (Fryirs 2013). At global scale (Broeckx et al., 2020) and more specifically in steep and mountainous regions (Larsen et al., 2014; Vanacker et al. 2015), landsliding is a dominant process of sediment mobilization and landscape denudation. Landslides processes are a dominant source of sediments (Korup et al. 2010) with the amount of material displaced being a function of their magnitude and frequency (Hovius et al. 1997; Crozier et Glade 1999; Malamud et al. 2004). At catchment scale, these stochastic processes can mobilize material that is either directly transported downstream or temporarily stored as colluvial fans on hillslopes. After rainfall events, debris flows can transport sediments to the fluvial system if the hillslope is physically linked to channels (Benda et Dunne 1997; Clapuyt et al. 2019).

To quantify the supply of sediment from landslides, the landslide mobilization rate (*LMR*) can be derived. This variable represents the volume of landslide material that is displaced per unit of area per year [m^3 km^{-2} yr^{-1}] (e.g. Guzzetti et al. 2009). The mobilization rate needs to be derived from complete landslide inventories that are covering a sufficiently long period and contain information about their respective sizes in combination with statistical relationships describing landslide size distributions (Hovius et al. 1997; Malamud et al. 2004; Guzzetti et al. 2009; Larsen et al. 2010) and empirical landslide area-volume relations (Larsen et al. 2010; Guns et Vanacker 2014). Because landslide mobilization rates are influenced by rare landslide-triggering events, the estimation of *LMR* requires sufficiently long periods of observation (Marc et al. 2015). Vegetation cover change can affect landslide frequency-area distributions as demonstrated by Guns and Vanacker (2014).

The contribution of landslide-derived sediment to the catchment sediment yield remains generally difficult to quantify (Hovius et al. 2000; Fuller et al. 2003). Much of the landslide-derived sediment is stored within catchments and does not directly contribute to specific sediment yields (*SSY,* [t km^{-2} yr^{-1}]). The latter represents the amount of material transported and evacuated out of a catchment (Broeckx et al. 2016, 2020). To improve the quantification and understanding of the landslide contribution to catchment sediment yield, processes driving the internal catchment sediment dynamics must be taken into account, e.g. sediment movements within catchments, presence of local storage, landscape connectivity and sediment (dis)connectivity of landslides within the catchment (Cook et al. 2020). Depending on the size of landslide and local topography, the displacement distance or runout length of mobilized landslides is mostly fall within the order of 1–1000 meters (e.g. Clapuyt et al. 2017; Rickenmann 2005). This could imply that most of the mobilized landslide material is deposited locally at foot slopes and in zero-order catchments while remaining disconnected from the river system for long periods (Hovius et al. 2000). Studies have shown that *SSY* generally decreases with increasing catchment area because of the increasing importance of sediment storage with increasing catchment area (Birkinshaw et Bathurst 2006; Vanmaercke et al. 2011; Larsen et al. 2014). Based on this, the *SSY/LMR* ratio is expected to decrease with increasing catchment size, given the increased storage opportunities for landslide-derived sediments (Broeckx et al. 2020).

Nevertheless, landslides and river networks constitute an important system of sediment production and transport (Hovius et al. 1997) but assessing its contribution to the sediment transport of river systems remains a key challenge to correctly predict the catchment sediment yields (Benda et Dunne 1997; Cook et al. 2020).

1.3. Sediment connectivity

The movement of sediment from source areas to the catchment outlet are "complex” (Fryirs 2013) because of issues linked to dynamics of sediment supply, processes of transfer between hillslopes and channels, to possibilities for deposition within catchments as well as spatial scales of erosion rates (Bracken et al. 2015). Landslides and sediment transport are also stochastic processes too. Therefore, quantifying the impact of landslide events on the sediment cascade or their contribution to erosion is a arduous task (Burbank et al. 2012; Berger et al. 2011; Clapuyt et al. 2019). One approach in assessing the contribution of each component of the sediment yield, is the concept of sediment connectivity.

In hydrological and geomorphological studies, landscape connectivity relates to the physical coupling of landforms (e.g. hillslope to channel) within a drainage basin (Bracken et Croke 2007; Hooke 2003). The connectivity of geomorphic systems can be defined by the water-mediated transfer of sediment between two different compartments of the catchment sediment cascade. Compartments are sediment stores or sinks to which sediment is added or removed through time. In catchments, three main types of linkages exist: longitudinal, lateral, and vertical. These linkages can interfere with blockage features termed buffers, barriers, or blankets. For example, lateral linkage can be characterized by the relationship between the slope-channel and the channel-floodplain. Landslide, gully, and alluvial fan stability can control the strength of this lateral linkage (Fryirs 2013).

Sediment connectivity is the connected transfer of sediment from a source to a sink in a system via sediment detachment and transport, controlled by how the sediment moves between all geomorphic zones in a landscape. In a catchment, those movements occur on hillslopes, between hillslopes and channels and within channels (Bracken et al. 2015). The hillslope-channel geomorphic coupling drives the response of the geomorphic system to sediment transfers (Clapuyt et al. 2019).

To apply the framework of sediment connectivity, it is necessary to establish a sediment budget, which measures the different sediment fluxes between sources and sinks. To construct a sediment budget, four main elements of the sediment conveyor belt must be quantified: delivery from sources (slope or valley floors), entrainment at critical shear stress, transport downstream (suspended load, bedload, or mixed load), and deposition in a temporal storage or more permanent sink. Landforms with short storage lifetimes are generally bars and banks, which are dependent on and characteristic of the river system. In contrast, slopes, floodplains and terraces are more permanent storage, where sediments remain in place for longer periods. Erosion, sediment transport and deposition occur at the grain scale, to produce landscape features at scales that are several orders of magnitude larger (Cooper et al. 2012). Interactions between these processes eventually control sediment flux at the catchment scale (Fryirs 2013).

To analyze hydrological and sediment connectivity, geomorphological and sedimentological field observations are commonly used (Bellin et al. 2009; Brown et al. 2009; Berger et al. 2011). An alternative is using geomorphometric indices based on digital terrain models. Geomorphic indices enable the identification of areas with potential for erosion, deposition and the linkage between them in landscapes. For example, Mitasova et al. (1996) proposed GIS-based methods for modeling the topographic potential for erosion and deposition with the Universal Soil Loss Equation (USLE) (Wischmeier et Smith 1978) as well as stream-power-based approaches. Borselli et al. (2008) developed a sediment connectivity index that showed good performance to define a hillslope sediment delivery ratio, i.e. the fraction of hillslope gross erosion that is delivered to the fluvial system. These models are based on similar approaches used in physical landscape evolution models, where sediment fluxes are derived by a linear or nonlinear relation with the hillslope gradient (Roering et al. 2001; Bishop 2007).

1.4. Methods to assess sediment budget in mountainous areas

In the study of mountainous landscape evolution and particularly mountainous environments, several data-oriented approaches help to assessing a sediment budget. Among others, cosmogenic nuclides as a long-term dating method, landslide mapping and connectivity indices are commonly used by geomorphologists.

1.4.1. CRN dating method for long-term quantification

In the last decades, cosmogenic radionuclides (CRN) have become a powerful scientific tool in Quaternary geochronology and landscape evolution studies (Ivy-Ochs et Kober 2008). By measuring CRN concentrations in rocks or sediments, the duration of exposure at or near the surface of the Earth can be assessed (Ivy-Ochs et Kober 2008). Cosmogenic radiation from outer space continuously bombards rocks and sediment. Interaction between cosmic radiation and elements in minerals located in the upper few meters of the Earth's surface produce stable (e.g. ^{3}He and ^{21}Ne) and radioactive (e.g. ^{10}Be, ^{14}C, ^{26}Al, and ^{36}Cl) nuclides (Bishop 2007).

The concentration of cosmogenic nuclides in rocks at the Earth's surface is linked to the rate of nuclide accumulation and rate at which the rock surface is being eroded (Burbank et Anderson 2012). The accumulation depends on the production rate governed by depth beneath the surface and varies with altitude, latitude and time (Granger et Riebe 2003). Once a rock is exhumed to the upper meters of the surface, the concentration of CRN in the material starts to increase due to cosmic-ray bombardment. Without erosion, the cosmogenic concentration constantly increases until reaching a "secular equilibrium". At this steady state, the concentration tends to remain constant. In the case of the rock being constantly eroded, the secular equilibrium is reached at lower concentrations (Burbank et Anderson 2012). The higher the erosion rate, the lower the radionuclide concentration at equilibrium (Figure 1A).

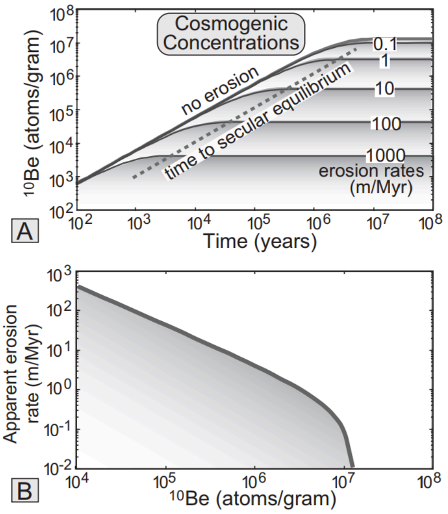

Figure 1 : Rock-surface erosion and cosmogenic concentrations (Burbank et Anderson, 2012).

The production of cosmogenic nuclides can be derived based on information on latitude, altitude and topographic exposure of the material. Knowing the production rates of the nuclides, the concentration of a particular isotope in a sample can be used to derive the surface exposure age (time since the sample has been exposed in the upper meters of the Earth's surface) when the erosion rate of the sampled surface is negligible (< 1 m Myr^{-1} or < 1 mm kyr^{-1}) since exposure. This is typically the case for exposed rock surfaces or large boulders. Combining several cosmogenic nuclides allows to verify this assumption.

When surface is eroded, the isotope concentration can be interpreted in terms of exposure age and erosion rate. By assuming that the surface is undergoing steady and uniform denudation, i.e. lowering, over a time period long enough to reach secular equilibrium, the isotope concentrations can be converted in denudation rates (Figure1 A). For more complex situations, numerical model approaches have been developed (e.g. Bishop 2007) that take multiple CRN concentrations into account.

At the catchment scale, the analysis of the cosmogenic radionuclide concentration of a sample of detrital quartz from the river sediment provides an average catchment-wide erosion rate over a millennial timescale. The assessment of the catchment-wide denudation rate is made under the assumption that quartz grains are derived from the entire catchment area and that tributaries contribute with sediment proportionally to their local erosion rate. As cosmogenic radionuclides integrate over hundreds to thousands of years, they provide mean denudation rates that are likely free of anthropogenic perturbations (Vanacker, von Blanckenburg, Govers, et al. 2007), in contrast to short-term measurements computed over years to decadal scale which may be subject to short-term fluctuations in erosion, weathering and land use (Granger et Riebe 2003; Burbank et Anderson 2012).

This technique is suitable to quantify exposure and denudation of rocks, soils and sediments over timespans of 1 kyr to 1 Myr, which is not possible with other dating techniques such as luminescence or radiocarbon dating. For example, luminescence dating cannot be used for coarse-grained material or sediments that have not been exposed to light long enough to trap sufficient energy. CRN dating method is also suitable to date organic-rich material that is older than the typical 50 kyr time span limitation of radiocarbon dating. Moreover, radiocarbon dating cannot be used to date sediment without organic matter (which is the case for most high alpine early Holocene or Lateglacial deposits). The wide variety of nuclides available (stable or with different half-lives) and the capacity to measure them in a variety of minerals allow the study of timing and rates of change of a large spectrum of landforms using cosmogenic nuclides (Ivy-Ochs et Kober 2008).

1.4.2. Landslide mapping for short-term quantification

A landslide is the movement of a mass of rock, debris, or earth down a slope, under the influence of gravity (Guzzetti et al. 2012). The general term “landslide” includes a range of slope movements, such as soil slip, deep-seated slides, mudflows, debris flows, rockfall, etc. (Varnes 1978). Triggering factors are rainfall, earthquakes, rapid snow melting, volcanic activity, and multiple human actions (Turner et Schuster 1996). This physical process develops through different stages over time: pre-failure deformations, failure itself and post-failure displacements (Hungr et al. 2014) (failure being the single most significant movement episode in the known or anticipated history of a landslide). A single failure can initiate a displacement or strain discontinuity and develop a ruptured surface. This rupture zone is discrete or distributed in a zone of a finite thickness (Tchalenko, J. S.; Morgenstern, N. R. 1967). After failure, the sliding material looses strength and the post-failure velocity of the landslide determines the change in the failure stage, from sliding to flow or fall (Hungr et al. 2014). The behavior and the type of landslides depend primarily on the type of movement and secondly on the material (Varnes 1978).

The increasing availability of digital topography due to recent technologies based on airborne satellite imaging (e.g. Light Detection And Ranging (LIDAR) and terrestrial remote sensing facilitates the study of topography (Passalacqua et al. 2015). Digital topographic representations enable to produce landslide inventories (Strozzi et al. 2010; Barboux et al. 2014; Tanyaş et al. 2017) where mapped areas are both the failure and runout areas. For complex slope movements, the boundary between the stable terrain and the failure or failed mass is transitional and often exhaustively fixed. In such case, the landslide failure area is difficult to determine with high precision (Malamud et al. 2004).

The quality of a landslide inventory depends on its accuracy and the type and certainty of the information contained. However, defining the accuracy of a landslide inventory is not straightforward. Accuracy depends on the completeness of the map as well as the geographical and thematic correctness of the information shown on it. Cartographic and geomorphic error are associated with the interpretation and transfer of landslide information between aerial photographs and digital mapping (Galli et al. 2008). The completeness refers to the proportion of landslides represented in the inventory in comparison to the real number of landslides in a study area (Guzzetti et al. 2012). Because the real number is usually unknown, the level of completeness of the inventory is also unknown. Furthermore, the completeness is directly linked to the minimum mapping unit which is the size of the smallest landslide that can be identified with a given method. Thus estimating the completeness of a landslide inventory is a difficult task (Guzzetti et al. 2012).

The number of landslides that occur with different sizes can be quantified by a frequency-area distribution. Based on empirical data of landslide inventories, previous studies (e.g. Hovius et al.,1997; Guzzetti et al., 2002, Malamud et al., 2004; Guzzetti et al., 2009; Larsen et al., 2010) have proposed that the frequency-area distribution of medium and large landslides follows a power law function (Figure 2). A power law function can describe any probability distribution of the form $p(x) = k\,x^{\beta}$. In a double logarithmic plot where $Y = log\,(p(x))$ is plotted against $X = log\,(x)$, the slope and the intercept of the regression line correspond to the unknown parameter values of β and $log\,(k)$. The slope is then known as the exponent or scaling parameter of the power law function (Clauset et al. 2009). This type of power law distribution is commonly applied to natural phenomena (e.g. earthquakes), and also landslides inventories (Hovius et al. 1997; Guzzetti et al. 2002; Malamud et al. 2004; Guzzetti et al. 2009; Larsen et al. 2010) as it allows the inclusion phenomena that differ in size, distribution, pattern, and triggering mechanisms (Malamud et al. 2004). The value of power law exponent β (scaling parameter) depends on the shape of the distribution and describes the power law decay for medium and large values. Therefore, the scaling parameter is a consequence of the studied landslide inventory. Several authors have shown that β is in the range of 1.0 - 3.3 for a variety of landslide inventories (Van Den Eeckhaut et al. 2007; Bennett et al. 2012; Tanyaş et al. 2018). For example, Hovius et al. (1997) computed β = 1.16 in the Southern Alps of New Zealand, Stark et Hovius (2001) β = 2.11 in Taiwan and 2.44 - 2.48 in New Zealand, Malamud et al. (2004) β = 2.40 in the Umbria region in Italy and Guzzetti et al. (2002) β = 2.50 in central Italy.

In addition, there is debate about the divergence of small landslides from the power law distribution in some inventories (Guzzetti et al. 2002; Malamud et al. 2004). The divergence refers to the point where the frequency-area value begins to decrease for smaller landslides following a positive power law decay (Figure 2). For non-cumulative frequency-area distributions, the point where the frequency density peaks is generally referred to as the cutoff point (Stark et Hovius 2001; Parker et al. 2015) or the rollover point (Malamud et al. 2004; Larsen et al. 2010). The rollover behavior can be related to underreporting of small landslides due to the mapping resolution (Stark et Hovius 2001; Bernard et al. 2020) but also to other issues linked to the physics of landsliding, landscape steepness (Katz et Aharonov

2006; Stark et Guzzetti 2009) and temporal resolution (Tanyaş et al. 2019). After testing several hypotheses on a variety of historical landslide inventories, Tanyas et al. (2019) concluded that the divergence for small-landslides from the power law distribution cannot be explained by a single factor. Because each inventory is different, Tanyas et al. (2019) have proposed that a combination of factors related to spatial and temporal resolutions of mapping and underlying failure process accounts for the deviation between landslide inventories and power law probability functions.

Malamud et al. (2004) analyzed three well-documented landslide inventories from Italy, Guatemala and California and found out that the probability density function of the landslide area is in good agreement with a truncated inverse-gamma distribution. Malamud et al. (2004) demonstrated that the rollover of the distribution for small landslides is real and cannot be explained as an artefact of inventory resolution. The distribution of small landslides in the three inventories shows an exponential rollover and medium and large landslides areas decay as a power law (characterized by a scaling exponent). Therefore, Malamud et al. (2004) proposed that the probability density of landslide areas is well approximated by a three-parameter inverse-gamma distribution:

$$p(A_L;\ \rho, a, s) \ = \ \frac{1}{a\Gamma(\rho)}\left[\frac{a}{A_L - s}\right]^{\rho+1} exp\left[-\frac{a}{A_L - s}\right] \qquad (1)$$

where $\Gamma(\rho)$ is the gamma function of ρ and A_L is the area of landslides.
The three parameters of the inverse-gamma probability distribution are (Equation 1):

- ρ controlling the power law decay for medium and large landslide areas,
- a controlling the location of the maximum probability distribution (rollover) and
- s controlling the exponential rollover for small landslide areas.

An inverse-gamma distribution $f(y)$ is obtained by making the substitution $x = 1/y$ into the gamma distribution $f(x)$. Fitting the three landslide inventories, Malamud et al. (2004) found empirical values for $\rho = 1.40$, $a = 1.28 \times 10^{-3}$ km^2 and $s = 1.32 \times 10^{-4}$ km^2 by maximum-likelihood optimization ($r^2 = 0.965$) (Equation 1). The value of $\rho+1$ equals to the scaling exponent β of the power law.

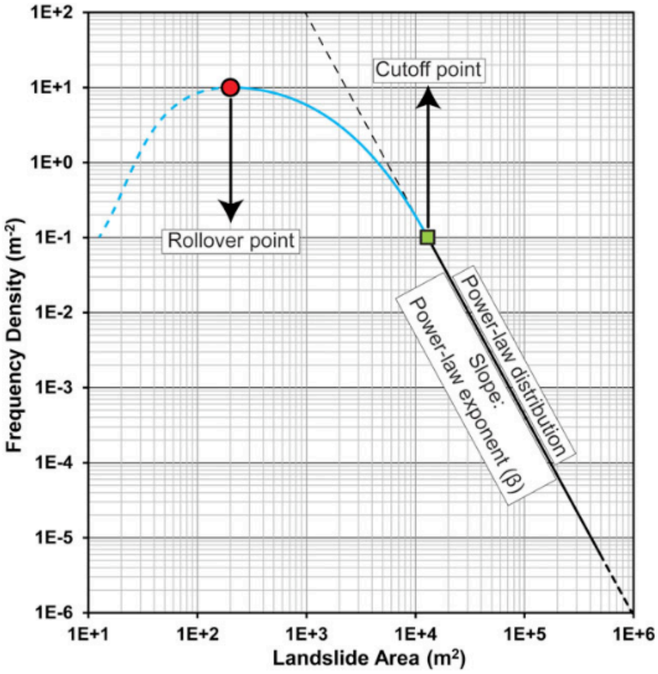

Figure 2 : Schematic of the main components of the non-cumulative from Tanyas et al. (2019).

Frequency-area probability distributions of landslides can be used as a proxy for the severity of landslide events and to study their spatial distribution (Malamud et al. 2004; Larsen et al. 2010; Broeckx et al. 2016). Given the typical semi-ellipsoidal form of landslides, the volume V of landslide-derived sediment can be determined from the landslide area A (Hovius et al. 1997; Larsen et al. 2010):

$$V = \alpha {A_L}^{\gamma} \tag{2}$$

where γ is the scaling exponent and $\log(\alpha)$ the intercept of the volume-area relationship. The relation can be empirically determined based on field measurements (Hovius et al. 1997; Guzzetti et al. 2009; Larsen et al. 2010). Larsen et al. (2010) have demonstrated that the scaling exponent depends on the type of the landslide. Based on a compilation of landslide geometry measurements from 4,231 individual landslides, Larsen et al. (2010) assessed that shallow and soil-based landslides can be approximated by an γ of 1.1-1.3 and other landslides which have deeper scar area (because involving the failure of bedrock) are characterized by a γ of 1.3-1.6.

The volume-area relationship enables the computation of the total volume of landslide material (*TVL*, [m³]) of a specific landslide inventory:

$$TVL = \sum_{i=1}^{n} V_i \tag{3}$$

where V_i is the individual landslide volume [m³] and n is the total number of landslides.

The landslide mobilization rate (LMR, [mm kyr^{-1}] or [m^3 km^{-2} yr^{-1}]) is computed as (Larsen et al. 2010):

$$LMR = \frac{TVL}{CA \times TS} \tag{4}$$

where TVL is the total volume of landslide material [m^3], CA is the catchment area [km^2] and TS the time span of a complete landslide inventory [yr].

1.4.3. Connectivity indices

In alpine catchments, the rough and irregular topography induces important variations in erosion and sediment delivery in the headwaters. It is the sediment connectivity between hillslopes and channels and along the channel network which drives the sediment flux at the outlet of mountainous catchments. The topographic representation of the surface was enhanced with the use of very high resolution digital terrain models (Bishop 2007), which improve the representation of drainage area, drainage pattern and surface roughness (Cavalli et Marchi 2008; Trevisani et al. 2010). Cavalli et al. (2013) improve the connectivity index of Borselli et al. (2008) by developing a sediment connectivity index (*IC*) to model sediment pathways including debris flows and channelized sediment transport, particularly for alpine environments. Cavalli et al. (2013) also adapted the workflow to a GIS environment to better exploit high-resolution digital terrain models (DTMs) in steep terrain. The developments of Cavalli et al. (2013) allow to limit bias in the *IC* derivation due to steep slopes. In an alpine environment, steep slopes are generally located close to rocky cliffs and bedrock channels where sediment mobilization occurs and storage is difficult (Cavalli et al. 2013).

Cavalli et al. (2013) applied the connectivity index (*IC*) on two adjacent catchments, i.e. Gadria and Strimm, located in the upper Venosta (Vinschgau) valley in the Italian Eastern Alps (Figure 3). The two maps were computed to represent the potential transfer of sediment from hillslopes to two different sink references: (1) the outlet (Figure 3a) and (2) the main channels and lakes (Figure 3b) of the catchment. The outlet reference allows the assessment of sediment connectivity until the outlet in order to analyze the export of sediments from the catchment. The main channel and lakes allow the study of sediment delivery from the hillslopes and zero order channels-tributaries until the main channel. A relatively high index means high connectivity and efficient sediment transfer by e.g. debris flows. In contrast, low values of connectivity index represent areas poorly connected to the outlet or other specific targets. Because of morphological conditions, glacial cirques, lakes, or other hillslopes areas can be decoupled from channels and so from sediment delivery to lower parts of the catchment (Cavalli et al. 2013; Figure 3).

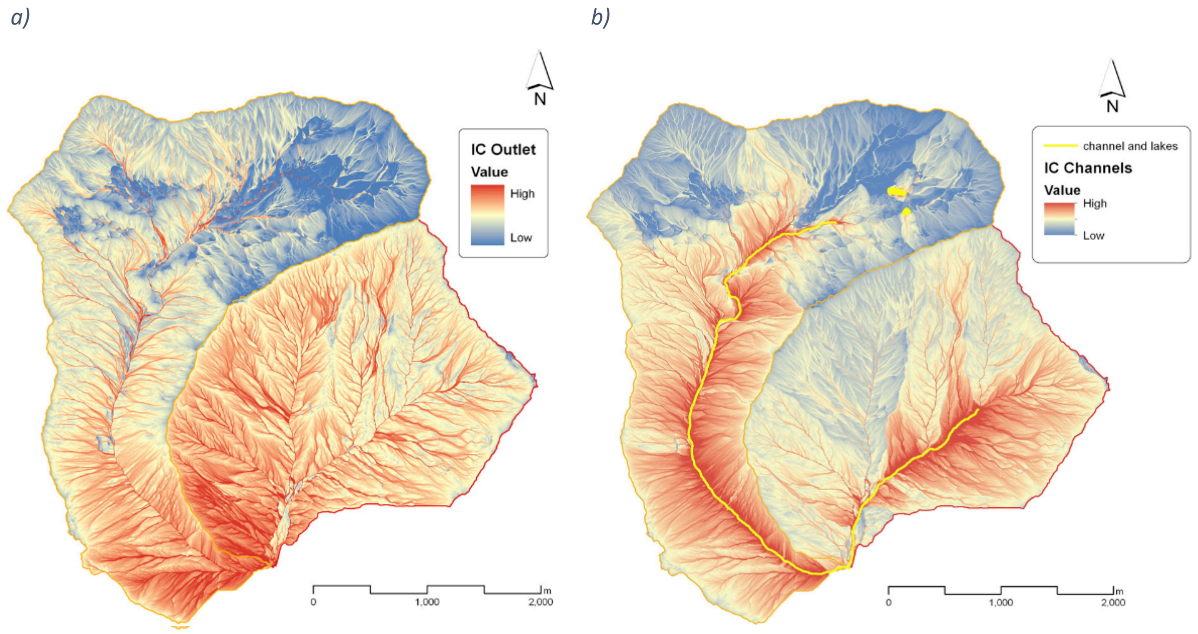

Figure 3: IC channels map computed with reference to: a) the outlet of the studied catchments and b) the main channels and lakes from Cavalli et al. (2013).

1.5. Research questions

Individual case studies have shown interesting results on denudation rates of alpine catchments, landslide-derived sediment fluxes and sediment connectivity (Hovius et al. 1997; Malamud et al. 2004; Ivy-Ochs et Kober 2008; Burbank et al. 2012; Cavalli et al. 2013). However, few studies have combined these three different datasets. There is a gap in the literature about the contribution of landslide-derived sediment to the overall sediment budget of mountainous regions.

Therefore, to improve the understanding of sediment dynamics at catchment scale (Figure 4) the objective of this study was to verify the two following hypotheses:

> (1) The landslide magnitude-frequency distribution of an alpine area is not dependent on the presence of glaciers in the headwaters. Catchments that are dominated by glacial processes show similar probability distributions of landslides as catchments dominated by fluvial processes.
>
> (2) The denudation rate of alpine catchments is dependent on the landslide mobilization rate in the headwaters. The contribution of landslide-derived denudation to the overall denudation varies as a function of the geomorphic processes in the headwaters, and the hillslope-channel connectivity.

The dataset for this study is composed of: orthophotos with 1 and 2.5 m of resolution[1] (2016), Digital Elevation Model (DEM) with 2 m of resolution[1] (2016), satellite images[2] (2007) and catchment-averaged denudation rates over late Holocene timescales (0.5-3 kyr) for some catchments in the upper Rhône Valley (Appendix 3) from Norton et al. (2010).

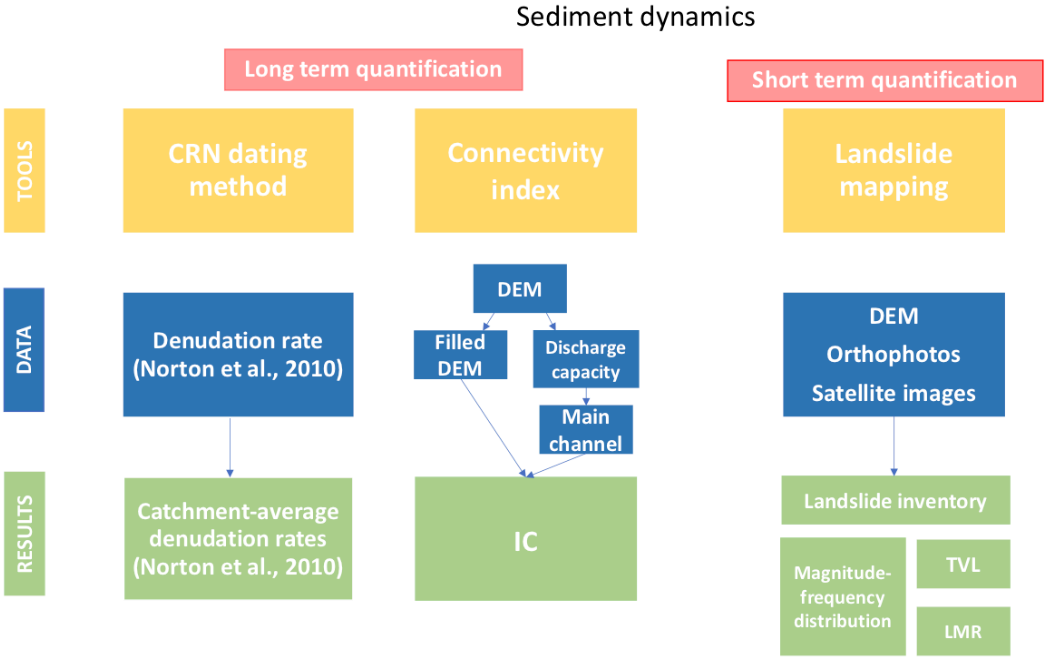

Figure 4: Methodological workflow applied in this study.

---

[1] SwissTopo open data repository (Federal Office of Topography swisstopo s. d.; https://www.swisstopo.admin.ch/en/geodata.html)

[2] Google Earth Pro 7.3.

2. Study area

The study area is composed of two river catchments located in the upper Rhône Valley in the Western Swiss Alps. The Rhône Valley is the largest inner alpine catchment which extends in the Canton of Valais between the Rhône Glacier and Lake Geneva with a size of 5,244 km^2 (Figure 5). The Rhône River originates from the Rhône Glacier (2,341 m asl) and crosses the Western Swiss Alps with a total length of 164 km; with a NE-SW direction upstream of Martigny and SSE-NNW direction downstream (Brandolini et al. 2020). Over the Quaternary period, the upper Rhône Valley was covered by some of the thickest alpine glaciers (Kelly et al. 2004). The Rhône Glacier filled the Upper Rhône Basin during the Last Glacial Maximum (LGM), around 22.1 kyr ago. From this LGM position, the deglaciation and retreat of western Alps glaciers started in 21.1 ± 0.9 kyr BP and ice collapsed between 16.8 and 17.4 kyr BP. (Schoch et al. 2018). The glacial and post-glacial processes shaped the topography of the upper Rhône catchment. The northern lateral tributary valleys parallel to the Rhône present effects of glacial erosion (Reynard 2009). The side valleys are separated by broad soil-mantled ridges. At lower elevations, triangular faceted surfaces are found between the streams. The side valleys with the highest elevation of the headwaters were occupied by valley glaciers until the current warm period of the Holocene. Where these glaciers were large, the valleys have been deeply scoured, with wide valley bottoms, U-shaped cross-sections, and steep valley walls. In all other side valleys of the upper Rhône Valley, Pleistocene glaciers were either too small to scour the main valleys or non-erosive, leading to cirque basins with post-glacial, fluvially incised lower reaches (Ustaszewski et Pfiffner 2008). After the last deglaciation, tributaries draining the side valleys developed large alluvial fans; which subsequently modified the trunk valley and covered relict traces of erosional processes (Reynard 2009). Currently, the Rhône is a strongly regulated Alpine river with an annual mean discharge of 1,720 m^3 s^{-1} at its mouth and a specific discharge of 17.8 l s^{-1} km^{-2} (Olivier et al. 2009).

Norton et al. (2011) computed denudation rates over late Holocene timescales (0.5-3 kyr) in the Eastern and Southern Alps. They measured concentrations of beryllium-10 (^{10}Be) in 37 samples of detrital quartz from 33 streams of the Eastern Alps of Northern Italy and Western Austria. For calculations, they used the scaling laws of Dunai (2000) and production equations of Schlatter et al. (2005). Two denudation rates assuming an initial exposure age of 15 kyr and cosmogenic steady state were estimated. To capture the maximum variability of each catchment, Norton et al. (2010) adopted a semi-random sampling scheme. The basin-averaged denudation rates range from 170 to 1,400 mm kyr^{-1} for the Eastern Alps (Norton et al. 2011). In a separate study, Norton et al. (2010) focused on 13 tributaries of the upper Rhône (Appendix 3) and derived denudation rates between 60.5 and 2,080 mm kyr^{-1}. The results show a difference of two orders of magnitude in denudation rates in the region, with glacial catchments having denudation rates between 760 to 2,800 mm kyr^{-1} and non-glacial catchments denudation rates between 60.5 and 560 mm kyr^{-1} (Norton et al. 2010).

Based on the results presented in Norton et al. (2010), we selected one glacial and one fluvial catchment. The outlets of the catchments are located around 110 km upstream of Martigny in the communes of Goms and Obergoms. They are located north of the Rhône River and underlain by the Aare Massif. The Aare Massif, which consists mostly of foliated gneisses with schists present in highly sheared zones (Labhart 1977).

The "Minstigerbach" (*Mins*) catchment has a total area of 15.4 km^2, a mean slope of 31° and a mean altitude of 2492 m. An upstream western part of the tributary basin is covered by the Minstiger glacier of ca. 2.17 km^2. This catchment is characterized as a glacial catchment and has a mean denudation rate of 2,120 ± 25 (steady-state) and 2,080 ± 25 (15 kyr) mm kyr^{-1}. (Figure 5; Federal Office of Topography swisstopo s. d.; Norton et al. 2010).

The "Niderbach" (*Nider*) catchment is located ca. 2.75 km to the East of *Mins* (Federal Office of Topography swisstopo s. d.) and drains a total area of ca. 3.4 km^2 with a mean slope of 29° and a mean altitude of 2,312 m. Three small lakes are present in the upper part of this fluvial catchment. *Nider 1* and *Nider 2* are two sub-catchments located in the upper zone of the catchment (Figure 8). *Nider* has a catchment-averaged denudation rate estimated at 218 ± 25 (steady-state) and 199 ± 25 (15 kyr) mm kyr^{-1}. For *Nider 1* and *Nider 2*, the denudation rates are 159 ± 17 and 144 ± 11 (15kyr) mm kyr^{-1} (Norton et al. 2010; Figure 5).

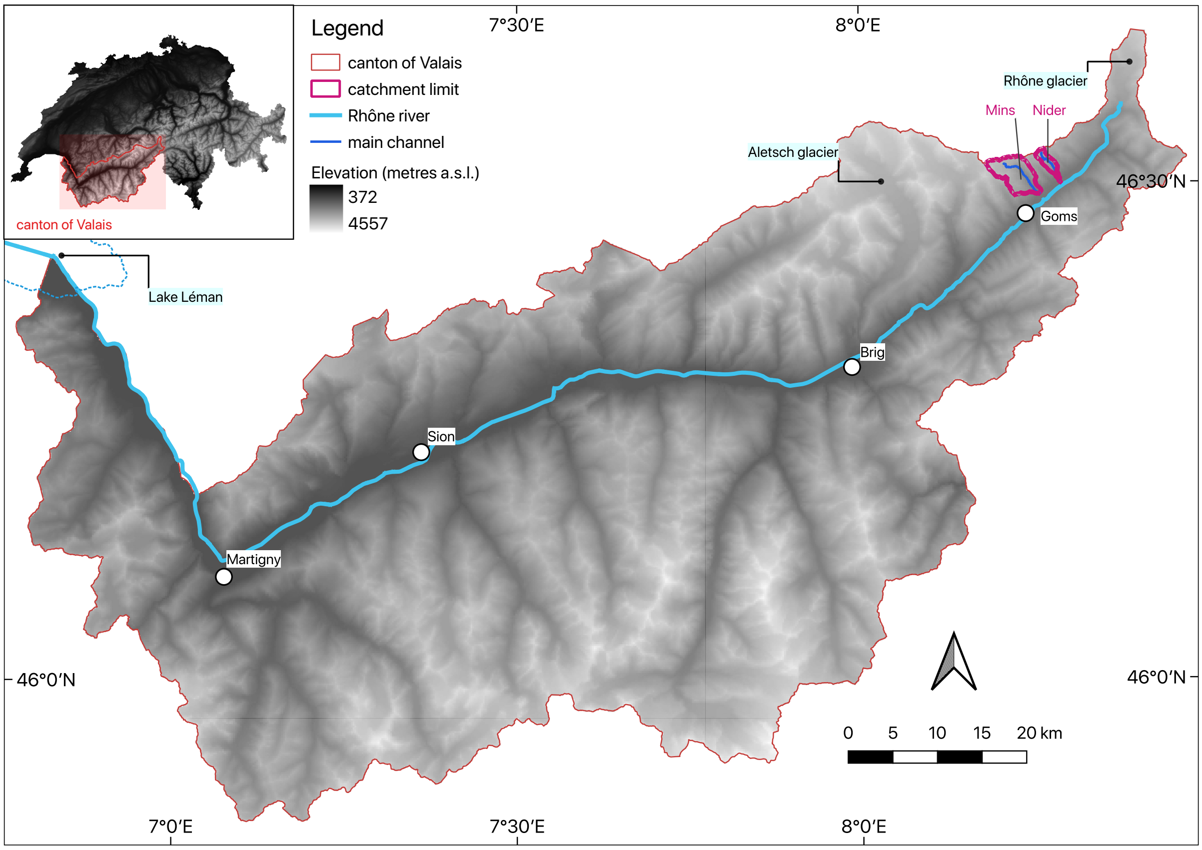

Figure 5 : Location map of the upper Rhône Valley, showing the canton of Valais with the two catchments Mins and Nider.

3. Material and methods

3.1. Compilation of landslide inventory

The core dataset of this study is based on an inventory of active landslides that was assembled for the two selected catchments. Primary data used for landslide mapping were:

- Orthophotos with 1 and 2.5 m of resolution (2016) from SwissTopo open data repository (Federal Office of Topography swisstopo s. d.; https://www.swisstopo.admin.ch/en/geodata.html)
- Digital Elevation Model (DEM) with 2 m of resolution (2016) from SwissTopo open data repository (Federal Office of Topography swisstopo s. d.; https://www.swisstopo.admin.ch/en/geodata.html)
- Satellite images (2007) from Google Earth Pro 7.3.

A historical landslide inventory consists of a single map including all landslide events that have occurred over a certain period. The landslides, reported in QGIS, were identified from data from 2007 and 2016. The Orthophotomosaic Swissimage (called “journey through time”) of Swisstopo allows to interactively explore the evolution of the landscape from 1976 to the present day for Switzerland. Based on it, all the landslides mapped in 2016 were also identified from 1976 to 2016 with fresh morphological appearance and very poor or absence of vegetation cover. Before 1976, aerial photographs were not taken as frequently over time and those available are not of sufficient resolution and quality to observe and judge the presence of these same landslides. However, in the literature, the probability of landslide occurrence over a hundred years is in the order of 0.5 to 1 (Guzzetti et al. 2005; Schlögel et al. 2015).

Each landslide that was identified based on the remote sensing data was characterized for its spatial extent (surface area) and its landslide type. Based on Varnes (1978) and Hungr et al. (2014), two main types were identified: rotational landslides and rockfalls. A rotational landslide is defined as a “sliding of a mass of homogeneous and usually cohesive soil on a rotational rupture surface with little internal deformation”. The velocity of this type of landslide is usually slow to rapid. The shape of the rupture surface of a rotational slump in cohesive soils is usually represented by cylindrical or ellipsoidal forms. However, in reality, the surface shape complexity depends on the type of material, permeability and saturation of the mass movement but also on the shape of the Earth’s surface beneath (Hungr et al. 2014). Rockfall refers to a mass of any size detached from a steep slope or cliff and along a surface on which little or no shear displacement occurs. The mass movement vary from very rapid to extremely rapid because the mass descends mostly through the air by free fall, leaping, bounding or rolling. The material of a rockfall especially comes from an area of bedrock and debris fall is composed of detrital fragments prior to failure (Varnes 1978).

Production of landslide inventory maps can be challenging because of difficulties in distinguishing clear boundaries between the failure areas and unaffected terrain, as well as identifying the type of landslide based on high-resolution remote sensing or topographic data.

The color, tone and texture of the satellite images depend on the light reflected by the surface, soil and vegetation types. To overcome this shortcoming, we used Google Earth satellite images. This second dataset helped us to clearly observe the surface characteristics, the type of material but also to check or find the exact limits of landslide features, to individualize or distinguish more complex landslide features (and avoid grouping single features). Other DTM-derived topographic variables, i.e. slope, aspect and hillshade, were also helpful to properly draw landslide extents.

To have consistent coverage, we defined the minimum mapping unit for the landslide inventory at 5 m^2. This corresponds to the size of the smallest landslide that was reported. Rockfalls and rotational landslides were mapped at the 1:500 scale and 1:200 for the smallest landslides. For each landslide feature, a polygon was drawn that corresponds to the affected area of single and active landslide features. The landslides dataset was produced in QGIS and the two catchment limits were computed using the LSDTopoTools software (Clubb et al. 2017).

3.2. Statistical analysis: magnitude-frequency distributions

The dependence of landslide frequency on landslide area is computed from the landslide inventory (Figure 10). The landslide probability density function is defined by Malamud et al. (2004) as:

$$p(A_L) = \frac{1}{N_{LT}} \frac{\delta N_L}{\delta A_L} \tag{5}$$

where:

- $p(A_L)$ is the landslide probability density which is the landslide frequency density, $f(A_L)$, divided by the total number of landslides in a substantially complete landslide inventory, N_{LT} .
- N_{LT} is the total number of landslides in an inventory.
- $\delta N_L / \delta A_L$ is the number of landslides with areas between A_L and $A_L + \delta A_L$.

The frequency density, $f(A_L)$ of landslide areas is the number of landslides δN_L with an area between A_L and $A_L + \delta A_L$ divided by a width of bin, δA_L. In this study, the nominal bin width for magnitude-frequency distribution computation was fixed at 20,000 m. The latter was transformed in order to obtain a constant in the logarithmic scale.

The fit of the landslide inventory distribution is a three-parameter inverse-gamma distribution (by maximum likelihood) (Equation 1; Malamud et al. 2004). This distribution is defined by the three parameters: ρ, a and s. The scaling exponent β representing the power law decay for medium and large values is associated to $\rho + 1$ and the rollover location is represented by a.

3.3. The estimated total volume of landslide material (and *LMR*)

Unlike a landslide area, landslide volume is not directly measurable using topographic data or aerial photographs. However, the empirical volume-area scaling relationship (Equation 2) helps to derive the landslide volume from the landslide-affected area (Hovius et al. 1997; Guzzetti et al. 2009; Larsen et al. 2010). Larsen et al. (2010) characterized this relationship (Equation 2) with the intercept $\alpha = 0.146$ and the scaling exponent $\gamma = 1.332$. These values were obtained empirically for small landslides with an area < 100 000 m^2 (Table 2) that mix bedrock and soil failures (Larsen et al. 2010).

By applying the empirical equation developed by Larsen et al. (2010) to our landslide inventory, we obtain the total volume of sediment that is mobilized by landslides, *TVL,* using equation 3. In this study, we used this volume to derive the landslide mobilization rates with equation 4, and made abstraction of the fact that the displaced material from the landslides can move downslope over a relatively short distance (Rickenmann 2005) and can be deposited on or at the bottom of the slope. As such, this volume of sediment is not necessarily completely removed, eroded from the failed slope or out of the catchment (Hovius et al. 1997; Guzzetti et al. 2009; Broeckx et al. 2020). Given that a multitemporal study was beyond the scope of this study, we defined two different time spans for the landslide inventory, *TS*, that equaled 40 and 100 yr. These values are based on analyses of aerial photographs (Federal Office of Topography swisstopo s. d.) and literature review (Guzzetti et al. 2005; Schlögel et al. 2015). A high landslide mobilization rate, *high LMR*, is related to a *TS* of 40 yr (between 1976 and 2016) and a low *LMR* to a *TS* estimated at 100 yr.

3.4. Connectivity index

Cavalli's sediment connectivity index (*IC*) represents the probability that sediment at a certain location of the valley will arrive in a specific sink (i.e. the outlet, the stream channel, etc.) by considering the small-scale hillslope morphometry. The *IC* values are defined and calculated locally for each raster cell of the high resolution DTMs (Borselli et al. 2008; Cavalli et al. 2013) as:

$$IC = log_{10} \frac{D_{up}}{D_{dn}} \tag{6}$$

where D_{up} and D_{dn} are respectively the upslope and downslope components of the connectivity (Figure 6).

The D_{up} is the potential for downward routing of the sediment that was produced upslope. D_{up} is calculated based on the values of the upslope contributing area, its average weighting factor W and its average slope gradient. The second component D_{dn} takes into account the flow path length that a particle has to travel to reach the nearest target or sink.

D_{dn} is calculated on each cell with the length of the flow path according to the steepest downslope direction, the weighting factor and the slope gradient (Cavalli et al. 2013).
To calculate contributing area, the Cavalli's *IC* tool uses the multiple flow D-infinity approach (Tarboton 1997) related to the cell size of high-resolution DTMs. Borselli's initial model defined a weight factor that is related to the impedance of the upslope and downslope components of the sediment cascade to runoff and sediment flux, and is related to land use and roughness. Borselli et al. (2008) used the C-factor of Revised Universal Soil Loss Equation (USLE-RUSLE) models to estimate soil impedance (Wischmeier et Smith 1978; Renard et al. 1997). However, in alpine catchments, large unvegetated areas are frequently observed. Therefore, a roughness index needs to reflect the resistance to sediment transport and transfer by e.g. debris flows. The surface roughness depends on the characteristics of outcropping rock and debris. As such, Cavalli et al. (2013) measured the topographic surface roughness as the standard deviation of the residual topography measured at a scale of few meters. The residual topography is then computed as the difference between the unsmoothed and smoothed DTMs derived by averaging DTM values using moving windows.

IC is defined in the range of $[-\infty, +\infty]$. Larger IC values mean higher connectivity (Cavalli et al. 2013).

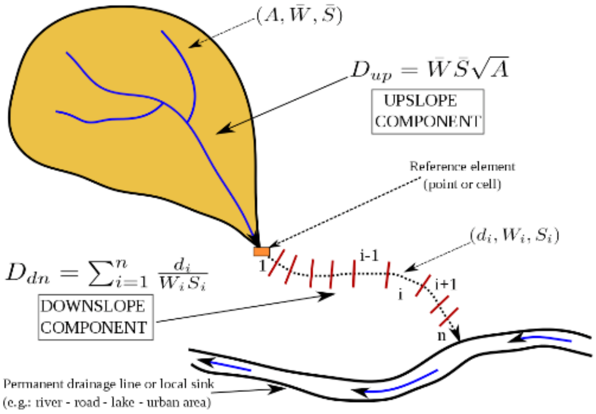

Figure 6 : Connectivity index upslope and downslope components (modified by Cavalli et al., 2013 after Borselli et al., 2008).

Using Cavalli's *IC* tool, we focused on two different aspects: (1) the sediment delivery across the whole drainage system to assess the potential connection between hillslopes and catchment outlets, and (2) the sediment coupling-decoupling between hillslopes and a selected main channel. We therefore aimed at assessing, respectively:

> (1) *IC outlet* as the probability that sediments from a given sediment source will reach the catchment outlet to get an idea of potential connection between hillslopes and catchment outlet and

(2) *IC channel as* the probability that sediment eroded from hillslopes will reach the main channel to observe where hillslopes sediments are potentially coupled or decoupled with the main channel.

The *IC outlet* was calculated with respect to the main channel of each catchment (Table 1). To derive the *IC channel*, a target feature was added in the *IC channel* workflow (Table 1). The adapted Cavalli's model was used in a stand-alone application, i.e. *SedInConnect*, implemented via a GIS procedure (Crema et Cavalli 2018). Input raster files used by *SedInConnect* are GeoTIFF format and input target features layer is a shapefile. Both *IC* indices were computed using the W weighting factor, demonstrated by Cavalli et al. (2013) as the surface roughness computed with the standard deviation of the residual topography from DTMs.

Table 1 : Input raster and shapefile files used in the SedInConnect application to compute IC index with respect to the main outlet (IC outlet) and with respect to the main channel (IC channel) for each alpine catchment Mins and Nider.

	IC outlet	***IC channel***
Input DTM raster (.tif)	filled DTM	filled DTM
Input cell size (m)	2	2
Input target polygon (.shp)	/	main channel

The main channels (used as the target in the *IC channel*) (Figure 7; Figure 8), were delineated in order to select the portion of the streams capable of effectively transporting eroded sediment. Firstly, the channel networks were computed with the SAGA QGIS Module "Channel network" for both *Mins* and *Nider* catchments (Figure 7; Figure 8), with the river initiation threshold of 50 000 m². Secondly, the two main channels were manually selected on the channel networks to analyze elevation and discharge capacity along them (Figure 7; Figure 8). The discharge capacity has been defined as (Whipple et Tucker 1999):

$$f\ (A^{m}\ \times\ S^{n}) \tag{7}$$

where A is the drainage area, S the slope gradient of the river and m = 1/3; n = 2/3.
A moving window of 40 m was used to derive the stream capacity (Equation 7; Figure 9). The profiles helped to determine where to cut and to select the portion of the main channels to use the more powerful portion as a target feature for the *IC channel*. In *Mins*, the discharge capacity highly increases downstream of the Minstiger glacier. Downstream of the front of the glacier (around 1.2 km downstream of the source), the discharge capacity looks almost constant (Figure 9a). This downstream part of the main channel was qualified as capable of effectively transporting eroded sediment and therefore selected as a target feature for the *IC channe*l (Figure 7). In *Nider*, two knickpoints appear around 0.8 and 1.3 km downstream of the source (Figure 9b). The second one is located at a lake. This lake plays the role of local base level for the stream where the water of the stream has less velocity and energy to erode and transport sediment. Downstream of this lake, the water starts again to flow with more velocity and energy. This is where the target channel feature has been cut (Figure 8).

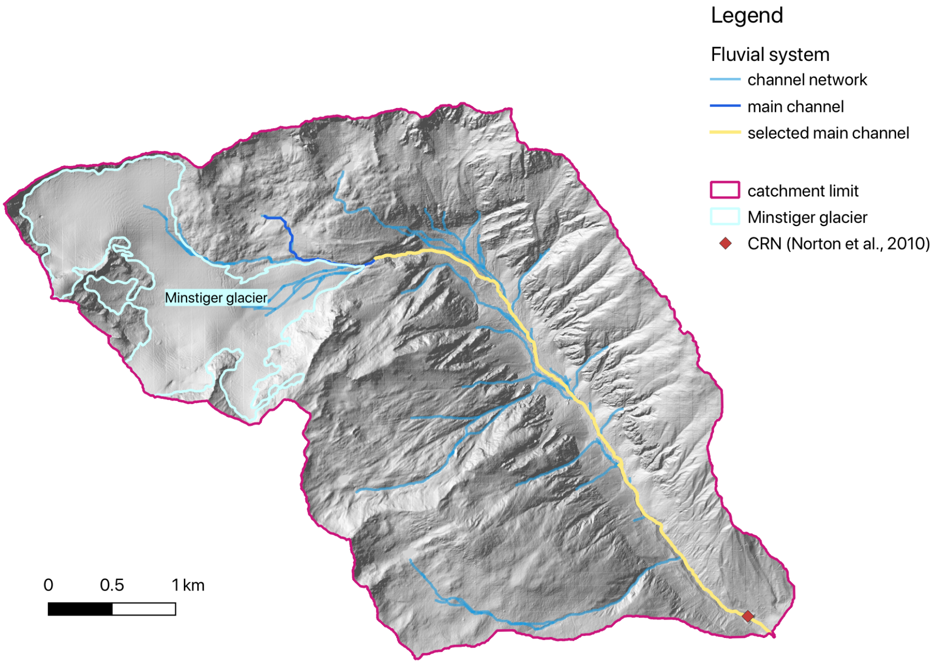

Figure 7 : Channel networks (computed with the SAGA QGIS Module "Channel network"; threshold value greater than 50 000 m²), main channels and selected main channels used for the IC index for the Mins catchment of the upper Rhône Valley. Background map : https://www.swisstopo.admin.ch/en/geodata.html.

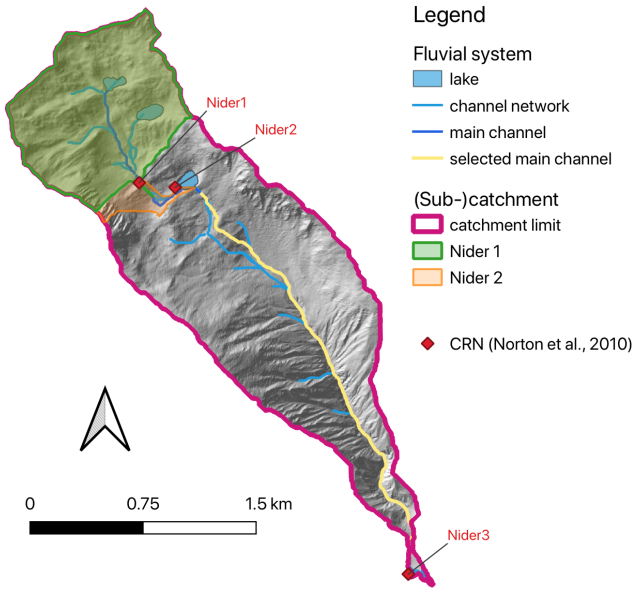

Figure 8 : Channel networks (computed with the SAGA QGIS Module "Channel network"; threshold value greater than 50 000 m²), main channels and selected main channels used for the IC index for the Nider catchment of the upper Rhône Valley. Background map : https://www.swisstopo.admin.ch/en/geodata.html.

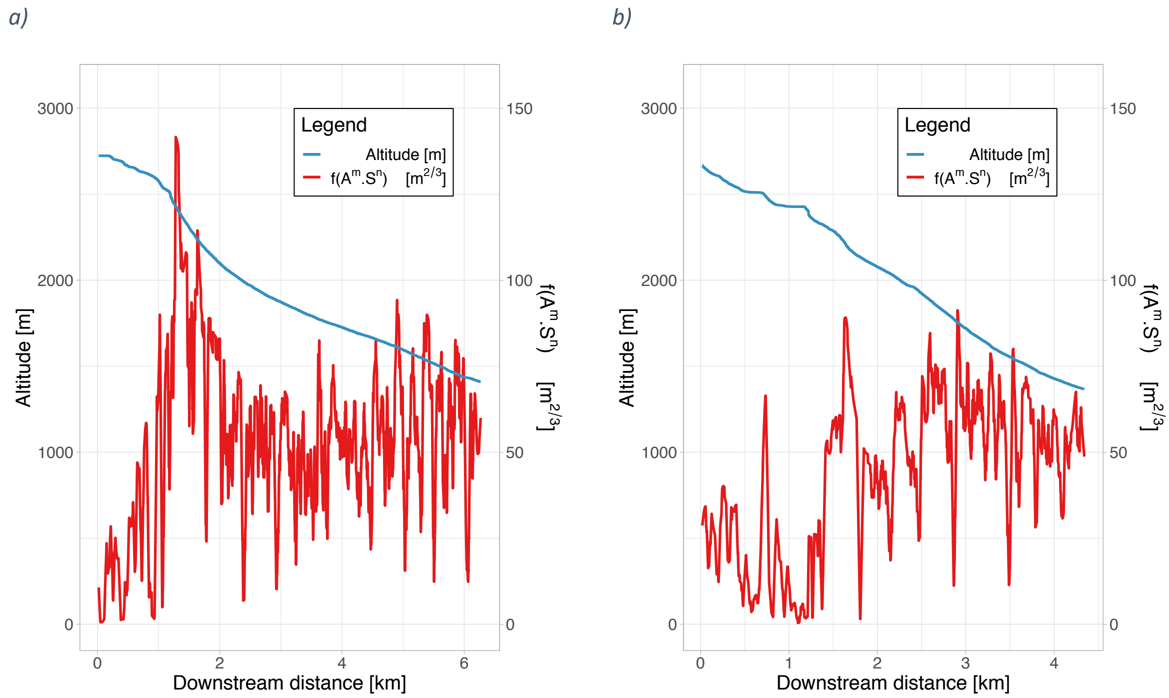

Figure 9 : Longitudinal profile and f(A^mS^n) (with a moving average window of 40 m) of: a) Mins (Figure 7) and b) Nider main channel (Figure 8).

4. Results

4.1. Landslide inventory and frequency-area distribution

The total number of landslides mapped is composed of 533 single features. In the *Mins* catchment, 374 landslides were mapped over a surface area of 15.46 km^2. They comprise 291 rockfalls of 6 to 93,392 m^2 that are mainly located in the headwaters of the catchment close to the glacier but also present on the lower slopes. In addition to falls, 83 rotational landslides with an area between 6 and 908 m^2 were mapped (Figure 10; Table 2).

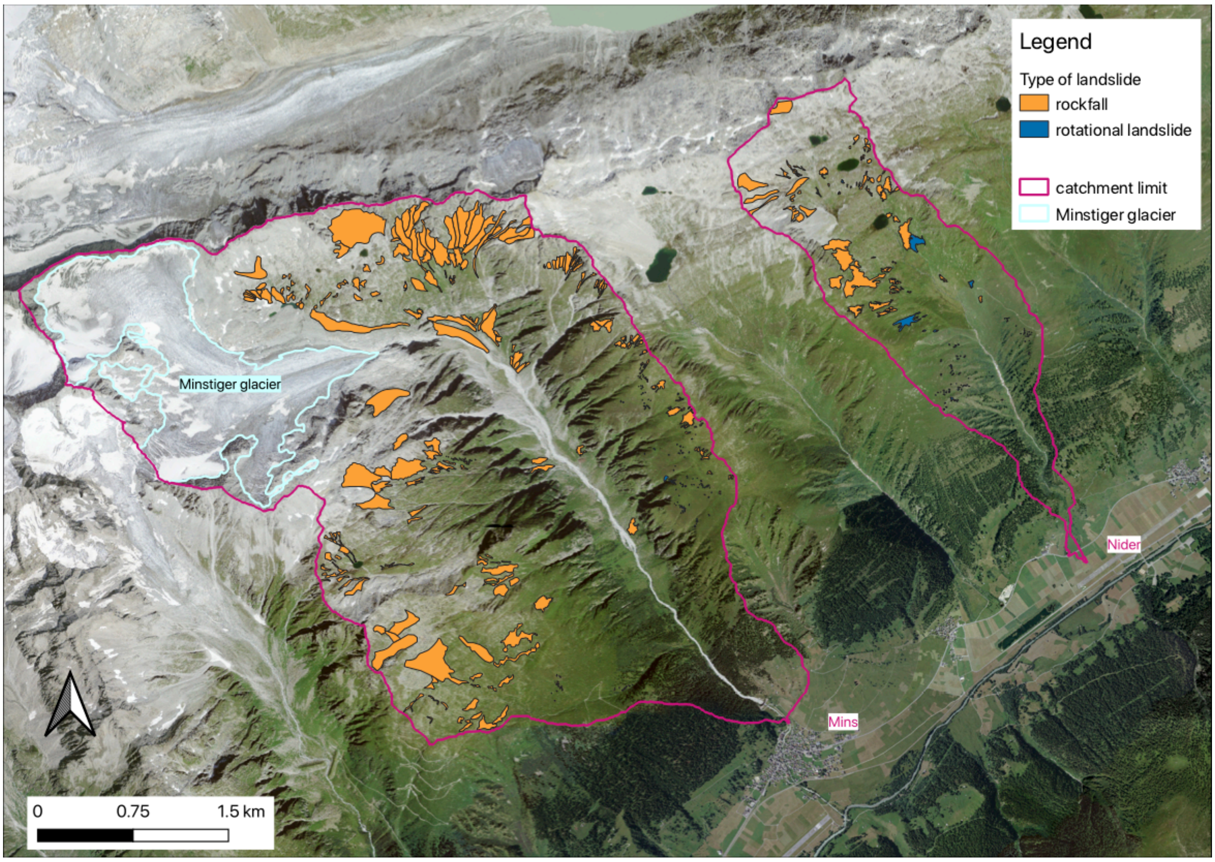

Figure 10 : The landslide inventory map for two tributary catchments located in the upper Rhône Valley, Swiss Alps. This map was produced based on orthophotos, digital elevation models and satellite image interpretation. This figure's location is shown in Figure 5.

The *Nider* catchment has 156 landslides over a surface area of 3.4 km^2. In this fluvial catchment, we mapped 73 rockfalls with an area between 59 and 29,314 m^2 and 83 rotational landslides between 5 and 8,880 m^2. Here, rockfalls were also primarily located at the foot of rock faces and further down the same slope. The rotational slides were smaller events (Appendix 1b), and mostly occurred in the lower part of the catchment (Figure 10).

The two landslide-area probability density distributions showed that small landslide (≤ 100 m^2) events were more frequent than big landslides (> 100 m^2) (Figure 11). Small landslides were mostly rotational landslides and bigger ones were rockfalls in the two catchments (Appendix 1; Appendix 2). Therefore, in the two catchments of the upper Rhône Swiss Valley, the probability to observe small-scale rotational landslides was higher than larger rockfalls. For the two catchments, the total surface area affected by landslides were about 0.07%. More rockfalls were mapped in the glacial catchment than in the fluvial catchment and more rotational landslides in the fluvial catchment than in the glacial catchment. The rockfalls density was about 0.077% and 0.059%, and the rotational about 0.0004 % and 0.0072 % for the glacial and fluvial catchments, respectively (Figure 11).

When fitting the inverse-gamma distribution to the data, the probability density functions of landslide area distributions $p(A_L)$ (Equation 5) showed a good visual match with a three-parameter inverse-gamma distribution (Equation 1; Figure 11). The residual standard error (*RSE*) was < 0.0015 and the three parameters were significantly different from zero (Table 2). These elements thus showed an equivalent fitting between the modeled and the observed values. The power law exponent β of the fitting was estimated at 1.29 ± 0.05 for *Mins* and at 1.18 ± 0.03 for *Nider* landslide inventory (Figure 11; Table 2). The rollover of the inverse-gamma a parameter, was: 15.38 and 5.75 for the *Mins* and *Nider* catchments, respectively (Table 2).

*Table 2 : Three-parameter inverse-gamma fitting of the landslide area distributions of the inventory (Equation 1) (*** p < 0.01).*

	***Mins* catchment**	***Nider* catchment**
Catchment area (km^2)	15.46	3.42
Total number of landslides, N_{LT}	374	156
Total number of rockfalls	291	73
Total number of rotational landslides	83	83
Total area affected by landslides (km^2)	1.20	0.23
Specific area affected by landslides (km^2/ km^2)	0.08	0.07
Specific area affected by rockfalls (km^2/ km^2)	0.0774	0.059
Specific area affected by rotational landslides (km^2/ km^2)	0.0004	0.0072
Mean area of landslides (m^2)	3,216	1,447
Smallest landslide area (m^2)	6	6
Largest landslide area (m^2)	93,392	29,314
ρ parameter	0.29 ± 0.05***	0.18 ± 0.03***
Power law exponent β	1.29 ± 0.05	1.18 ± 0.03
***a rollover location* (m^2)**	15.38 ± 3.21***	5.75 ± 1.42***
s parameter (m^2)	0.97 ± 1.17	3.26 ± 0.53***
Residual standard error of fit	0.0010	0.0014

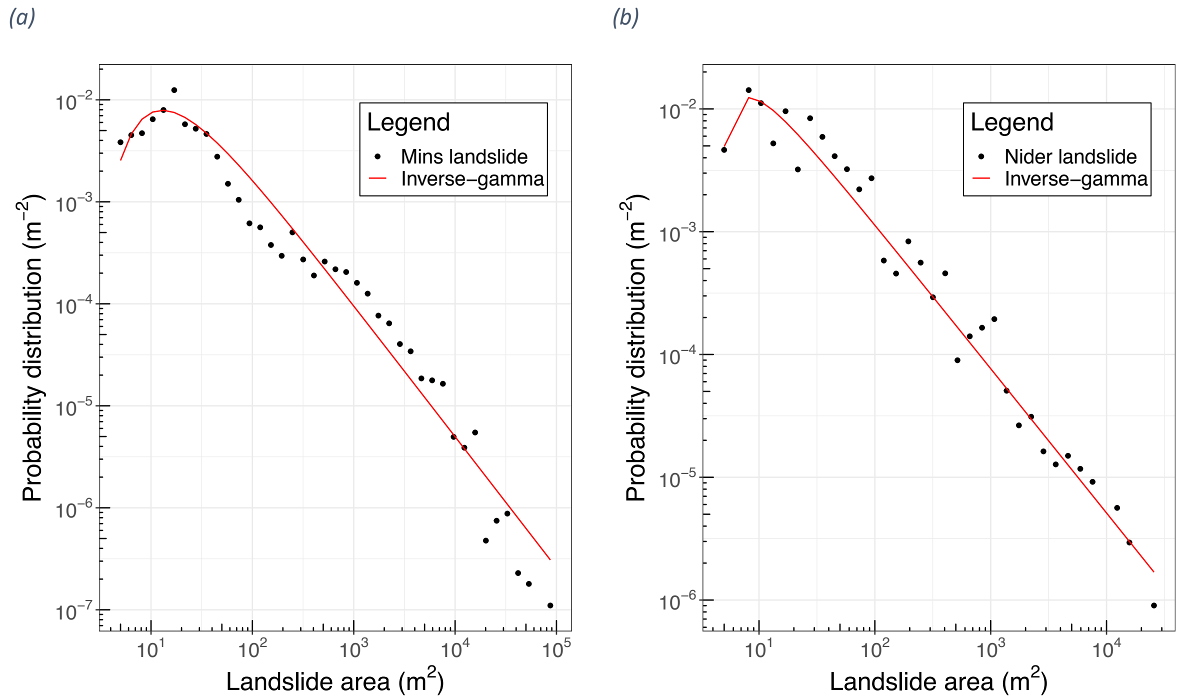

Figure 11: Landslide probability density $p(A_L)$ *(Equation 5) as a function of landslide area* A_L *for: a) Mins and b) Nider landslide inventory on logarithmic axes. The red line is the best 3-parameter inverse-gamma fit (Equation 1) of this distribution by maximum likelihood optimization with parameter values: (a)* $\rho = 0.29 \pm 0.05$, $a = 15.38 \pm 3.21$, $s = 0.97 \pm 1.17$ *(RSE: 0.0010 on 37 degrees of freedom) for Nider and (b)* $\rho = 0.18 \pm 0.03$, $a = 5.75 \pm 1.42$, $s = 3.26 \pm 0.53$ *(RSE: 0.0014 on 30 degrees of freedom) for Mins.*

4.2. Landslide mobilization rates (and denudation rates)

The total volume of landslide material mobilized (*TVL;* Equation 3; Larsen et al. 2010) in *Mins* was ca. 4.23*10^6 m^3. Based on this estimated volume of landslide-derived material, we calculated a high and a low mobilization rate (*LMR*) assuming that the time span of observations (*TS*) is about 40 yr and 100 yr. For *Mins*, we obtained a value of 6,837 for the high, and 2,735 mm kyr^{-1} for the low *LMR* (Table 3). When comparing the *LMR* with the catchment-averaged denudation rate (*DR*) published by Norton et al. (2010), i.e. the *LMR/DR ratio*, we observe that *LMR values* were in a range between 1.3 and 3.3 times higher than the denudation rates (Table 3).

In *Nider* catchment, the *TVL* was around 6.53*10^5 m^3. For the high and low LMR, we obtained 4,771 and 1,909 mm kyr^{-1}. Therefore, its *LMR/DR ratios* were about 24 and 9.6 times higher than the denudation rate. For both sub-catchments, the *TVL* was close to 2*10^5 m^3. The range of high and low *LMR* values was ca. 5,380 - 2,152 mm kyr^{-1} for *Nider 1* and 6,052 - 2,421 mm kyr^{-1} for *Nider 2.* Over these two sub-catchments, the *LMR-DR ratio* were the highest; on average the *LMR* were about 29 times higher than the denudation rates (Table 3).

The *TVL* was 6.5 times higher in the glacial catchment than in the fluvial catchment, which is not surprising given the 4.5 times larger surface area of *Mins* compared to *Nider*. Moreover, the *LMR* was also 1.4 times higher for *Mins* than for *Nider*. However, these LMR were almost of the same order of magnitude over *Mins* catchment and *Nider* sub-catchments.

Based on these results, the *LMR* of sediments mobilized by landslide processes were more important than the denudation rate over a thousand years at catchment scale; and even higher in the fluvial catchment as compared to the glacial catchment (Table 3).

Table 3 : Denudation rate (Norton et al. 2010), estimated TVL (Equation 3) and LMR (Equation 4) for (sub)-catchments. High and low LMR are respectively related to an inventory time span of 40 yr and 100 yr.

	Catchment area [km^2]	**Denudation rate [mm kyr^{-1}]**	**TVL [m^3]**	**High LMR [mm kyr^{-1}] [m^3 km^{-2} yr^{-1}]**	**High LMR/DR**	**Low LMR [mm kyr^{-1}] [m^3 km^{-2} yr^{-1}]**	**Low LMR/DR**
Mins	15.46	2,080 ± 940	4.23*10^6	6,837.05	3.29	2,734.82	1.31
Nider	3.42	199 ± 25	6.53*10^5	4,771.35	23.98	1,908.54	9.59
Nider 1	0.97	159 ± 17	2.10*10^5	5,379.62	33.83	2,151.85	13.53
Nider 2	1.05	144 ± 11	2.54*10^5	6,052.00	42.03	2,420.80	16.81

4.3. Connectivity index (IC)

The sediment connectivity indices showed that the *Mins* catchment is relatively homogeneously connected to the outlet and the main channel (Figure 13; Figure 14). The low standard deviations of the *IC channel* and *IC outlet* demonstrate this constant connectivity through the catchment (Table 4). These results show that sediments from different locations within the *Mins* catchment have the same probability to get to the outlet or the main channel. However, an exception is observed for the area located north of the Minstiger glacier, upstream of the source of the main channel. There, the *IC outlet* (Figure 13) and the *IC channel* (Figure 14) are higher than in the rest of the glacial catchment. The Minstiger glacier is also well connected to the main channel (Figure 14; 5.4).

The sediment connectivity index of *Nider* divides the catchment into two parts (Figure 13; Figure 14). This spatial pattern is even stronger for *IC channel* (Figure 14; Figure 12d) than *IC outlet* (Figure 13; Figure 12b). This is illustrated by the relatively high value of the standard deviation of the *Nider IC channel* compared to the other *IC* (Table 4). This difference in potential sediment connectivity is also well observed on the histogram (Figure 12b; Figure 12d). The upstream is poorly connected to the main channel, while the downstream is characterized by a higher connectivity to the main channel (Figure 14). The poorly connected area is located upstream of the lake which represents a local base level for the stream, and a barrier for the sediment connectivity within the catchment. Sediments upstream this local base level have a low probability to reach the main channel or the outlet (Figure 13; Figure 14).

The index maps (Figure 13; Figure 14) show different patterns of sediment connectivity in the two catchments. In the glacial catchment, most of the sediments are quite homogeneously connected the outlet or the main channel (Figure 13). In the fluvial catchment, the sediment connectivity index divides the catchment into two parts: upstream area is highly connected whereas downstream area is poorly lowly connected to the outlet and the channel (Figure 14). Most of the *Nider* potential sediment sources are also better connected to the main channel than *Mins* sediment sources. This can be illustrated by the important differences in the value of the third quantile of *IC channel.* The value of the third quantile of *IC channel* is -1.78 for *Nider* and -3.39 for *Mins* (Table 4). In addition, both *IC outlet* and *IC channel* suggest that the tributaries of the main channel are highly connected to the main channel as well as the outlet (Figure 13; Figure 14). Based on *IC channel,* we also observe that areas close to any part of the channel network are also well connected; and areas close to the trunk stream even more (Figure 14).

Table 4 : Main statistics of the sediment connectivity index with respect to outlets (IC outlet) and main channel (IC channel) of the two study catchments.

	Minimum	Maximum	Mean	Standard deviation	Median	First quantile	Third quantile
IC outlet							
Mins	-6.56	3.38	-3.66	0.83	-3.68	-3.91	-3.41
Nider	-6.49	3.01	-3.51	0.92	-3.37	-4.01	-3.09
IC channel							
Mins	-6.36	2.87	-2.73	0.74	-2.75	-3.22	-2.29
Nider	-6.41	2.59	-2.70	1.19	-2.39	-3.87	-1.78

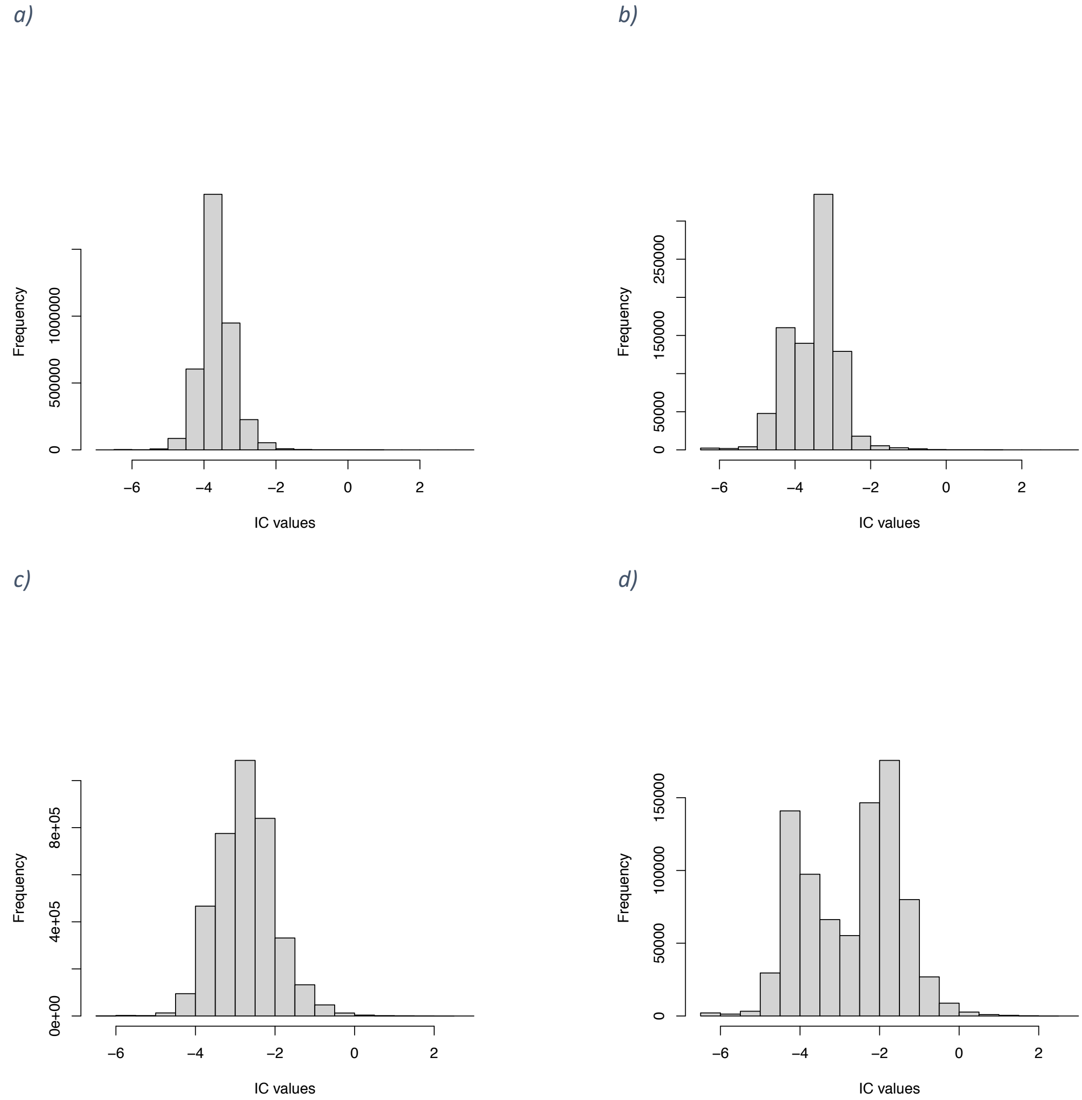

Figure 12 : Distribution of IC values per catchment: a) Mins IC outlet, b) Nider IC outlet, c) Mins IC channel and d) Nider IC channel.

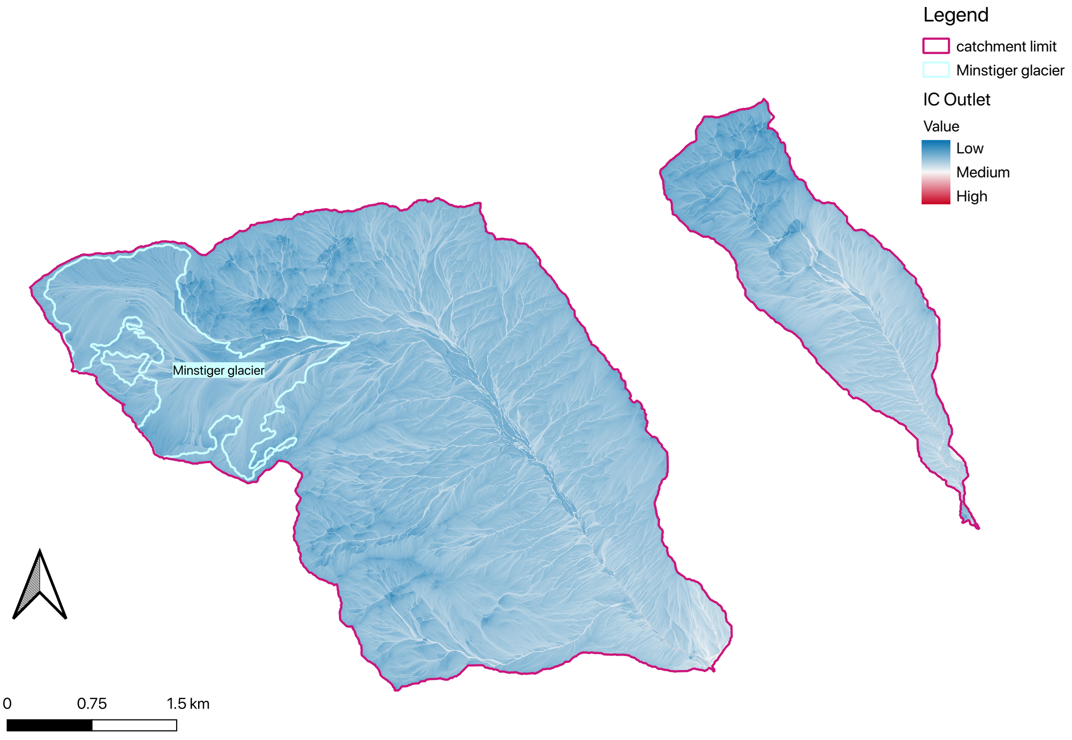

Figure 13 : IC outlet as an index of connectivity computed with reference to the outlet of the studied catchments. IC values are classified by equal interval.

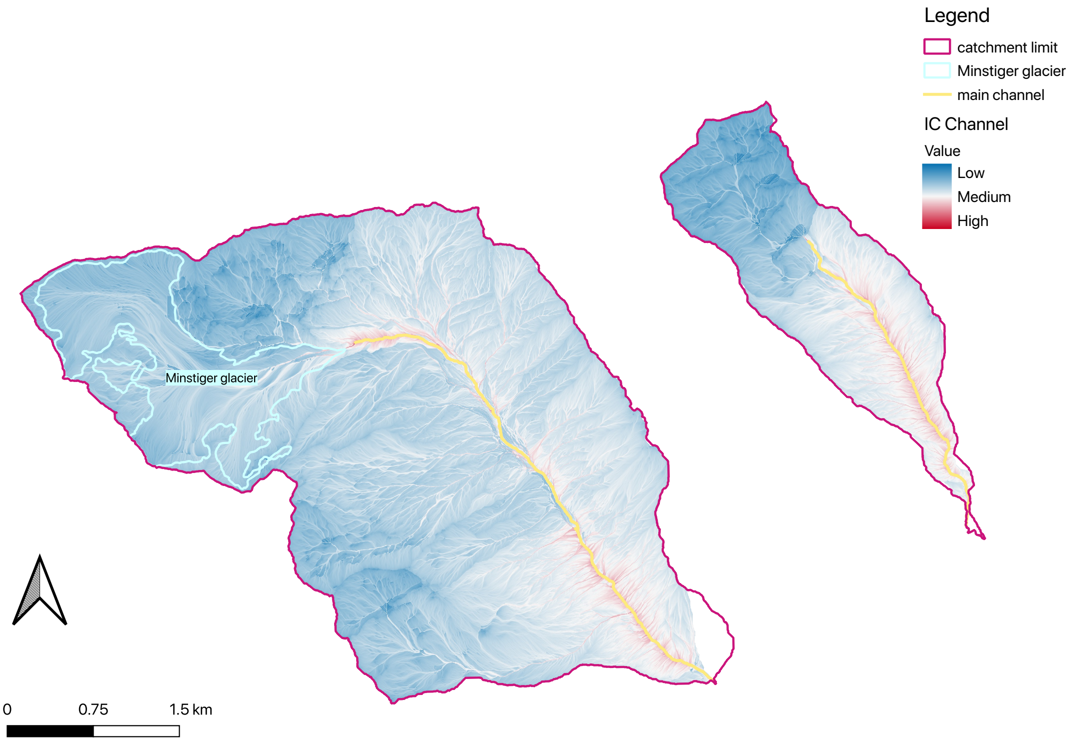

Figure 14 : IC channel as an index of connectivity computed with reference to the main channel of the studied catchments. IC values are classified by equal interval.

5. Discussion

5.1. Landslide inventory and magnitude-frequency statistics

The statistics about landslide magnitude-frequency are based on the landslide inventory maps that were created from very high-resolution orthophotos and DEMs (1 or 2 m resolution) from Swisstopo. This data allowed us to digitalize landslides with a minimum mapping unit of 5 m^2 and to define accurately their area, shape, location and type. Producing a historical inventory of landslides at this spatial scale and with this minimum mapping unit is time-consuming.
For a landslide inventory to be complete (Malamud et al. 2004), it is necessary to analyze all types of geomorphic features and digitize them on a topographic map. This is an arduous task in practice as other types of mass movements occur in alpine catchments (more specifically in the glacial catchment), where ice-avalanches are difficult to detect and digitalize. However, the amount of sediments produced by ice avalanches can be significant in such an environment. This work combined with a field study could help in verifying the presence of avalanches (and ice content) and potentially adding it consequently to the digitalization. However, the high-resolution data and fixed minimum mapping unit enable to produce an accurate and complete inventory.

Moreover, as the inventory is also composed of rockfall and rotational landslide types, it could also be used in the future to carry out field measurements that allow the differentiation of landslide types. For example, it would allow to check if the two empirical area-volume relationships (Larsen et al. 2010) are different depending of rockfalls and rotational landslides, and so that landslides mobilized different volumes of material compared to their area (Equation 2).

To verify the time span relevant for the inventory, we analyzed orthophotomosaics provided by Swissimage, and concluded that almost all the mapped landslides were active between 1976 and 2016. To have an accurate measure of the activity of mass movements, we were able to analyze the activity of each feature based on a time series analysis of SAR Interferometry (InSar) data (Barboux et al. 2014; Kenner et al. 2014). Radar interferometry can locate changes in the Earth's surface by analyzing of the interference pattern caused by the difference in phase between two images acquired by a spaceborne synthetic aperture radar. The two images must be obtained from two distinct times (Massonnet et Feigl 1998). The displacement rate of moving areas can be estimated by the interpretation of a differential SAR Interferometry (DInSAR) dataset. In a study of the Western Swiss Alps, the DInSar-detected movements showed a displacement rate ranging from a few centimeters to several meters per year and were attributed to various types of mass wasting phenomena, e.g. rock glaciers, landslides, etc. (Barboux et al. 2014). Dynamic and mean velocity information could be integrated in this study in order to understand the dynamic processes in mountain areas. Such information would improve the understanding of the impacts of slope mass movements on sediment dynamics in alpine catchments. Moreover, accurate kinematical data can help to locate potential areas of erosion or deposition in a mountainous environment.

The *Mins* and *Nider* landslide probability density distributions (Figure 11) followed a power law shape with a rollover behavior for small landslides. The divergence of small landslides from the distribution was accepted and well fitted with a three-parameter inverse-gamma, as proposed by Malamud et al. (2004). Estimated by the best model of this distribution (Table 2; Equation 1), the two power law exponents of the *Mins* and *Nider* landslide area distribution were 1.29 ± 0.05 and 1.18 ± 0.03, respectively. Our results are in good agreement with values previously published in the literature, i.e. ranging from 1.16 to 2.4 (Table 5; Hovius et al. 1997; Stark et Hovius 2001; Guzzetti et al. 2002; Malamud et al. 2004). However, the two power law exponents of *Mins* and *Nider* (1.29 and 1.18) are in the lower range of previously published values. This indicates that *Nider* and *Mins* have a relatively low number of large and medium landslides but, a higher number of small landslides in comparison to landslide inventories characterized by β = 2.40 (Malamud et al. 2004) or β = 2.50 (Guzzetti et al. 2002). In addition, the rollover locations in this work are also lower than those found in the literature, which are ca. 10^{-3} km^2 (Hovius et al. 1997; Guzzetti et al. 2002; Malamud et al. 2004) or 10^{-4} km^2 (Stark et Hovius 2001). For *Mins* and *Nider*, the most abundant landslide areas were about 15 m^2 ($15*10^{-6}$ km^2) and 6 m^2 ($6*10^{-6}$ km^2), respectively, and thus smaller than generally found in the literature. As a comparison, Hovius et al (1997) obtained a size value of 5,000 m^2 for the most frequent landslide for their inventory in the Southern Alps in New Zealand, Malamud et al. (2014) of 1,300 m^2 in Italy, and Guns and Vanacker (2014) presented a range between 102 m^2 and 123 m^2 in Ecuadorian Andes (Table 5).

Table 5: Power law exponents of different inventories published in the literature.

Autor (Study area)	**Power law exponent β**	**Rollover location (a) (km^2)**	**Landslide area range (km^2)**
(Hovius et al. 1997) (Southern Alps, New Zealand)	1.16	$5*10^{-3}$	10^{-3} - 10^{0}
(Stark et Hovius 2001) (Taiwan)	2.11	$5*10^{-4}$	10^{-5} - 10^{0}
(Stark et Hovius 2001) (New Zealand)	2.44-2.48	$8*10^{-4}$	10^{-4} - 10^{-1}
(Guzzetti et al. 2002) (central Italy)	2.50 ± 0.5	$2*10^{-3}$	10^{-3} - 10^{-1}
(Malamud et al. 2004) (Umbria, Italy)	2.40	$1.3*10^{-3}$	10^{-5} - 10^{0}
(Guns et Vanacker 2014) (Andes, Ecuador)	2.00-2.43	$1.02*10^{-4}$ - $1.23*10^{-4}$	$1.2*10^{-5}$ - $1.1*10^{-2}$
This work (Swiss Alps, *Mins*)	1.29 ± 0.05	$15*10^{-6}$	$5*10^{-6}$ - $9*10^{-2}$
This work (Swiss Alps, *Nider*)	1.18 ± 0.03	$6*10^{-6}$	$5*10^{-6}$ - $3*10^{-2}$

The relatively high occurrence of small landslides in the inventory is probably related to the minimum mapping unit that was used in this work (Table 5). Indeed, the mapped landslides had surface areas of several m^2 to hm^2 (10^{-6} - 10^{-2} km^2), while in the literature values generally range between several dm^2 to km^2 (10^{-4} – 10^{0} km^2). Most data sources do not allow mapping landslide areas smaller than 10^{-4} km^2 and are omitted from the literature (Hovius et al. 1997; Stark et Hovius 2001; Guzzetti et al. 2002). In this case study, the high resolution of the digital photographs and the limited extent of the study area allowed us to include them in the inventory. To conclude, the frequency distribution of landslide areas and the power law exponent seem to be controlled by the minimum mapping unit.

5.2. Landslide mobilization rates

In *Mins* catchment, the high landslide mobilization rate (*LMR*) was estimated at 6,837 mm kyr^{-1} and the low *LMR* at 2,735 mm kyr^{-1} (Table 3). In the *Nider* catchment, we observed lower values than in the Mins catchment with high and low *LMR* of respectively 4,771 and 1,909 mm kyr^{-1} (Table 3), respectively.

Other previously published LMR values have also been computed based on landslide inventories. For the Alps, the mean *LMR* has been estimated at 2,700 mm kyr^{-1} (Broeckx et al. 2020). For catchments in Italy, Guzzetti et al. (2005, 2009) calculated a range of LMR values between 1,447 and 2,509 mm kyr^{-1}, and Brardinoni et al. (2020) obtained values of ca. 1,917 mm kyr^{-1}. As a consequence, the low *LMR* (Table 3) of *Mins* and *Nider* fits well within the range of published values for the Alps. The low *LMR* values were based on a time span of the landslide inventory (*TS*) that was fixed at 100 yr. Even if the *LMR* is higher in the glacial than the fluvial catchment, the *Mins* low *LMR* (2,735 mm kyr^{-1}) remains very close to the mean *LMR* of the Alps (2,700 mm kyr^{-1}; Broeckx et al. 2020). In contrast, the high *LMRs* (6,837 for *Mins* and 4,771 mm kyr^{-1} for *Nider*; Table 3) related to *TS* of 40 yr seems higher than the aforementioned mean *LMR* value of the Alps (Broeckx et al. 2020).

5.3. Denudation rates

Catchment-averaged denudation rates for *Mins* and *Nider* catchments have been reported to be of 2,080 ± 940 and 199 ± 25 mm kyr^{-1}, respectively (Norton et al. 2010). It shows that the denudation rate in the glacial catchment is ca. 10 times higher than the fluvial catchment. The surface covers of the two catchments is different, with heterogeneous rock and vegetation cover. The surface of the Mins catchment is covered by bedrock (23%), debris (15%), glaciers (18%) and soil (43%). In the *Nider* catchment, the surface cover is mainly soil (77%), as well as bedrock (6%) and debris (17%) (Norton et al. 2010). The type of erosion processes and transport depend on the surface cover. Compared to *Mins*, the high percentage of surface area covered by soil and vegetation (77%) in the *Nider* catchment enhances soil stability and reduces the susceptibility to erosion processes. In addition, the high *Mins* denudation rate is related to the relatively high percentage of debris surface cover and the presence of a glacier in the uppermost glacial catchment (Norton et al. 2010; Figure 7). Indeed, the Minstiger glacier potentially enhances the occurrence of specific glacial erosion processes, i.e. ice-avalanches, rock glacier, solifluction lobes, etc.

Rock glaciers are composed of a mix of various-size rock particles which, under a few meters of non-permanently frozen rock debris (i.e. the active layer) are cemented by interstitial ice (Kummert et Delaloye 2018). This debris landform is generated by a creep of frozen ground and conveying debris from an upslope area (source area or rooting zone) towards their front (Delaloye et Morard 2019). Active rock glaciers move at low speed, i.e. typically
0.1 to 2 m yr^{-1} (Delaloye et Morard 2019). The deformation of the ice explains the downslope movement of a rock glacier. This deformation concentrates mostly in one main shear horizon 15-30 m deep or in some cases, in several of them located above the main one (Kummert et al. 2018; Delaloye et Morard 2019). Lugon (2010) demonstrated that (an increase of) the permafrost creep at the Ritigraben rock glacier (Valais, CH) became an important sediment source for debris flows over the last few decades. This increase of the movement rate of the rock glacier is induced by a general increase of the mean temperature and seems to occur everywhere in the alpine arc (Lugon 2010; Kenner 2018; Kummert et Delaloye 2018). The net debris production and amount of annual sediment delivery from the rock-glacier body into the upper part of the debris-flow channel has been estimated between 100 and 700 m^3 yr^{-1} depending on the direction of the rock-glacier (Lugon 2010). However, a direct coupling between rock-glacier and debris-flow processes, and torrential events in the fluvial system is difficult to establish. This is due to a temporal gap between the actual sediment production at the front of the rock glacier and the entrainment of the accumulated material by debris flows (Lugon 2010; Brardinoni et al. 2020). Immediate feedbacks may exist in a period of extensive precipitation events. Rainfall events lead to active-layer detachment and failure at the snout of the rock glacier (Lugon 2010).

When comparing the *LMR* with the catchment-averaged denudation rate (*DR*) published by Norton et al. (2010), i.e. computing the *LMR/DR ratio*, we observe that ratios are larger for the fluvial than for the glacial catchment (Table 3). In the *Nider* catchment, the *LMR-DR* ratio was about 24 for the high *LMR* and 9.6 for the low LMR in comparison to 3.3 and 1.3 in the *Mins catchment* (Table 3). For both sub-catchments (Figure 8), the *TVL* was close to $2*10^5$ m^3. The high and low LMR values were about 5,716 and 2,289 mm kyr^{-1} on average for *Nider 1* and *Nider 2*, respectively, as compared to 4,771 and 1,909 mm kyr^{-1} on average over the entire catchment*.* Therefore, over these two sub-catchments (Figure 8), the *LMR-DR ratio* were the highest, i.e. ca. 37.5 for the high *LMR and* ca. 15.5 for the low *LMR* (Table 3). These differences of *TVL*, *LMR* and *LMR-DR ratio* between *Nider* sub-catchments and catchment (Figure 8; Table 3) can be explained by the hypothesis stating that the lakes located in the uppermost part (Figure 8) play a role in sediment storage for upstream sediments on the long term. The *TVL* was on average three times lower, but the *LMR* ca. 1.2 and *LMR/DR ratio* ca. 1.6 higher for both sub-catchments, than over the entire catchment on average (Table 3).

The denudation rates calculated by Norton et al. (2010) are based on cosmogenic nuclide concentrations in stream sediments at the outlet of the catchments. These rates are catchment-averaged values and do not allow the detection of spatial variations in denudation rates within the catchments. To obtain insights about the spatial patterns of denudation rates, a sampling along the channel network is required (Brardinoni et al. 2020). In the fluvial catchment, it was performed for two upstream sub-catchments (Figure 8). These two denudation rates are 159 ± 17 mm kyr^{-1} for *Nider 1* and 144 ± 11 mm kyr^{-1} for *Nider 2*. This information revealed that the two *Nider* upstream areas have a lower denudation rate than the entire catchment (199 ± 25 mm kyr^{-1}; Table 3). For the glacial catchment, only the outlet sample and the associated catchment-averaged denudation rate are available (Figure 7; Norton et al. 2010). A detailed sampling in the upper part mainly covered by the glacier and the downstream part, which has already experienced deglaciation, would allow the exploration of spatial patterns in denudation rates.

In the upper Rhône Valley, denudation rates of the lateral valleys, dissecting the north and the south sides of the Rhône, vary from 61 to 2,080 mm kyr^{-1} (Figure 15; Appendix 3). The highest rates are found in the two glacial catchments *Mins* and *Rec* and the lowest in the fluvial valleys. These two glacial tributary catchments are still currently glaciated in their uppermost parts (Norton et al. 2010).
Moreover, a clear difference is observed in denudation rates for catchments located north and south of the Rhône river. The mean denudation rate is 447mm kyr^{-1} for glacial and fluvial north valleys and 218 mm kyr^{-1} for only fluvial north valleys (Figure 15; Appendix 3). In the south valleys, Norton et al. (2010) studied five fluvial valleys with an average denudation rate of 752 mm kyr^{-1} (Ritz, Spi, Ch, Bet and Löü; Figure 15; Appendix 3). The fluvial north valleys are less eroded than the fluvial south valleys. The northern tributaries of the Rhône river drain the Aare Massif and the southern tributaries the Gotthard Massif. Despite differences in lithological composition, the two massifs are mainly composed of gneisses and schists (Labhart 1977). Moreover, Norton et al. (2010) discussed and rejected a lithological control on the denudation rates. An alternative explanation of the difference in denudation rates between the northern and the southern catchments could be related to the slope morphology and the exposure to solar radiation. Indeed, solar insolation partially controls hillslope asymmetry and the slope orientation influences the angle at which the sun's rays strike the surface, and therefore the collected solar energy and the slope temperature. In the Northern Hemisphere, the surface temperature is generally higher and the vegetation cover is present further upstream in south-facing than north-facing hillslopes (Pelletier et Swetnam 2017).
Large drainage areas, presence of glaciers, high relief, abundant exposed bedrock and prevalence of debris flows have been demonstrated as driving elements for high denudation rates in this region. However, it is difficult to attribute variations in denudation rate to one or several of these causes, as elements may be interrelated and difficult to study independently (Norton et al. 2010).

To conclude, the method used to estimate the denudation rate at the catchment scale can be refined. Norton et al. (2010) determined denudation rates assuming steady-state erosion over the last thousand years. This assumption of constant and uniform weathering and erosion over the past 13,000 years, might not apply in deglaciating areas. Besides, the concentration of cosmogenic nuclides in river sediment can be sensible to short-term fluctuations (over years to decades) in sediment supply and transport. Over short time scales, deep-seated landslides and rockfalls can supply sediment that is depleted in cosmogenic nuclides to the river network and affect the derivation of catchment-averaged denudation rates (e.g. Clapuyt et al. 2019) .

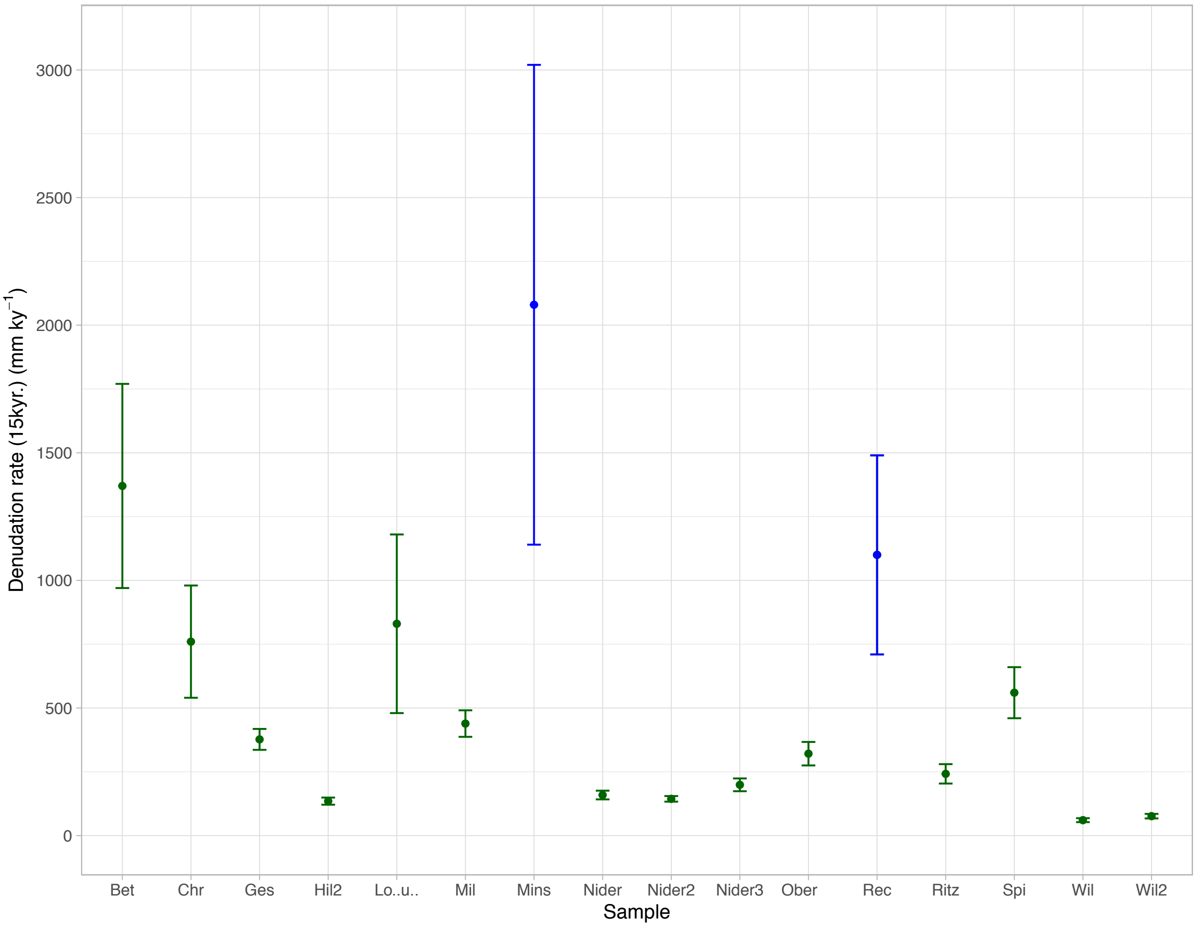

Figure 15 : Catchment-averaged denudation rates of fluvial (in green) and glacial (in blue) catchments of the upper Rhône Valley (Norton et al. 2010). Location of the selected catchments are shown in Appendix 3.

5.4. Sediment connectivity indices

The indices of sediment connectivity (*IC*) of the two catchments (Figure 13; Figure 14) show the relevance of applying the Cavalli et al. (2013) scheme to estimate sediment connectivity in alpine environments. The analysis of the *IC channel* (Figure 14) is quite different and more illustrative than the *IC outlet* (Figure 13).

The *Mins IC channel* showed that sediments from the entire catchment have a similar probability to reach the main channel (Figure 14). This *IC channel* slightly improves the connectivity of some areas along the main channel and near the glacier compared to the *IC outlet*. This improvement of connectivity to the main channel may be possible after a deglaciation period. It might illustrate the potential coupling of the sediment sources present in the glaciated area with the channel network in a future deglaciated time. Outside the Minstiger glacier and nearby areas, the upper parts of both slopes of the glacial catchment are poorly connected to the main channel, whereas the lower slopes near the main channel are highly connected (Figure 14). The connectivity varies along the main channel. Around halfway of the channel, where the river morphology is anastomosing and partly covered by thick alluvial deposits, the hillslopes are less connected to the channel than in other sections (close to the source and outlet) where the channel is confined (Figure 14; Figure 10).

The *Nider IC channel* divides the catchment into two parts (Figure 14; Figure 16). The upstream part of the catchment is only dominated with low *IC* values, representing a relatively low connectivity to the main channel. The lower part has higher *IC* values indicating that sediments have a higher probability to be better connected to the main channel (Figure 14). The upper sector includes the upper hanging valley, shaped by past glacial activity and actual periglacial processes with gentle slopes. The sediment delivery to the main channel is very limited, despite a lack of vegetation cover and the presence of thick sediment covers initially mobilized in the upper steep rock slopes (Cavalli et al. 2013). The three lakes constitute effective barriers to downstream sediment routing. Large colluvial features and thin but long rockfalls (Figure 10) cover the *Nider 1* and *Nider 2* floodplains (Brardinoni et al. 2020). These characteristics of the upper part of the catchment and the lake as sediment sink or storage are well illustrated by the higher *LMR* of *Nider 1* and *Nider 2* compared to the entire *Nider catchment* (Table 3). The lowermost sector (Figure 16) is characterized by higher *IC* values and a lower spatial variability (Figure 14) where the *Nider* main channel flows through a very steep, narrow gorge. In this lowermost and more vegetated part of the catchment (Figure 10), the transfer pathways from the ridge to the main channel are straight, steep and rather short (Figure 8; Figure 16). Indeed, the sediment supply of sediment from hillslopes to the channel network depends on active erosion processes (Cavalli et al. 2013). However, in this sector of the catchment, the vegetation cover stabilizes the hillslopes, thus reducing their susceptibility to erosion processes and lateral sediment transfer during ordinary rainfall events (Cavalli et al. 2013). Along the main channel extended over a relatively long distance of 3.25 km, on the other hand, both the morphology and the relative connectivity slightly differ. These variations in the fluvial morphology depends on the number, size and steepness of colluvial channels, and thickness of colluvial deposits (Brardinoni et al. 2020; Cavalli et al. 2013) on adjacent hillslopes in this lower sector (Figure 16). This *Nider* division (Figure 16) is quite similar to sectors 1 and 3 of the geomorphological division developed by Cavalli et al. (2013) for the Strimm catchment (Eastern Alps, Italy; Appendix 4).

When interpretating the *IC outlet* (Figure 13), we clearly see that hillslopes and the outlet of the catchment are coupled, which makes the sediment delivery efficient. This sediment coupling may hide small areas of deposition (i.e. sediments deposited around and in the lakes) and present the Minstiger glacier as poorly connected to the outlet (Figure 13). Nevertheless, the presence of lakes in the two catchments is relatively well represented. Indeed, lakes are characterized by with very low *IC* values, indicating that they are poorly connected and decoupled from the outlets (Figure 13) or the main channels (Figure 14).

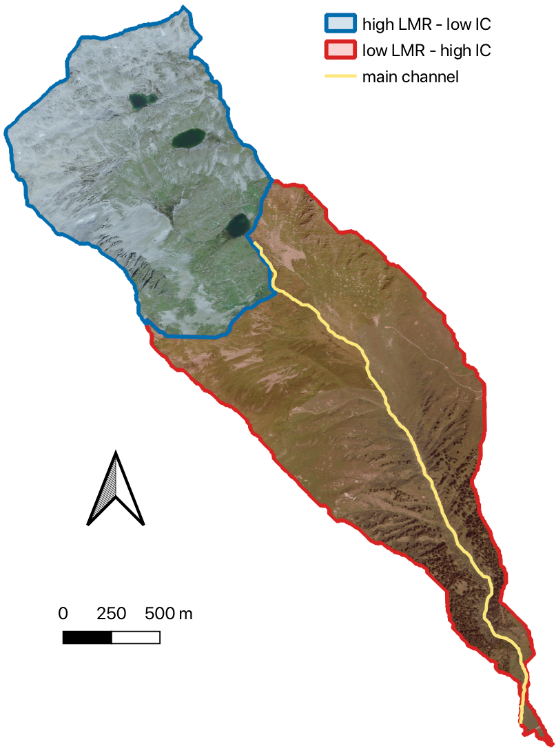

Figure 16 : Division of the Nider catchment into two sectors according to the values of the LMRs and IC.

Cavalli et al. (2010) adapted the *IC* in order to take include the presence of deposition processes such as debris flows and channelized sediment transport. However, it does not take into account the whole spectrum of processes modulating sediment transfer in mountain areas. The improvement of the weighted *W* and slope *S* factors were not particularly optimized for other hazardous events such as ice-avalanches or rockfalls. The specificity of the study area, e.g. the importance of rockfalls (and the possibility to add ice-avalanches in the glacial catchment), could be taken into account in the improvement of a new *IC* index.

Moreover, in the fluvial catchment, the *IC outlet* and *IC channel* show the same *IC* spatial variation between the upstream and downstream parts (Figure 13; Figure 14; Figure 16). However, the patterns of connectivity between the *IC outlet* and *IC channel* are slightly different in the glacial tributary (Figure 13; Figure 14). Considering the specificity of sediment production and transfer in the fluvial and glacial domains would increase the representation of the sediment connectivity for alpine environments (although it might compromise the simplicity of this GIS-model). In its present state, the proposed model of Cavalli et al. (2013) appears suitable for a rapid spatial characterization of sediment connectivity related to the transfer processes (i.e. debris flow and channelized sediment transport) in the alpine catchments. Nonetheless, it appears clearly more adapted for fluvial ones.

5.5. Comparison and relation between the main results: magnitude-frequency distribution, denudation rate and sediment connectivity

The magnitude-frequency distributions of the landslide inventory are well fitted by an inverse-gamma distribution. In addition, both distributions also confirm the idea of the divergence of small landslides from the power law distribution (Figure 11). These results suggest that in the fluvial and also glacial catchments, small landslides appear more present than medium and large ones. Based on the inventory, landslide areas were converted into volumes (Equation2) in order to assess landslide mobilization rates (Table 3). If we disregard that the sediment cascade is *perfect* and that landslide mobilized material is efficiently transported to the outlet, we can observe that the *LMR* values are ca. 1.5 times higher in the glacial catchment than in the fluvial one (Table 3). Then, larger LMR values are observed when compared to the denudation rates that integrate over the millennial timescale. This points to the importance of landsliding as an erosion process at the catchment scale. Nevertheless, connectivity and sediment transfer between hillslopes and channel network in alpine catchment are hard to study (Bracken et al. 2015) and efficient connectivity does not always ensure an effective downstream transfer of sediment (Cavalli et al. 2013).

In order to improve the understanding of this sediment connectivity, the *IC* indices (Cavalli et al. 2013) were computed with the outlet (Figure 13) or the main channel (Figure 14) as targets. The *IC* results demonstrate spatial patterns of sediment connectivity, which can be related to the denudation rate and the sediment flux. In the fluvial *Nider* catchment, the two sub-catchments have higher rates of *LMR* than for the entire catchment (Table 3) on average. Sediment connectivity to the main channel and the outlet of these two upstream areas is lower than the downstream part of *Nider* (Figure 13; Figure 14). Sediments that are produced in the two upstream sub-catchments have thus a low probability to be routed to the main channel and outlet because of this low potential connectivity. Therefore, there is a decoupling between the sediment produced in these upstream parts of the catchment, and the sediment dynamics in the lower parts that control the catchment-averaged denudation rates. This observation also illustrates the role of the three upstream lakes and the tributaries of the main channel located upstream (Figure 8). Indeed, rivers draining the upstream parts of the catchment transport sediments to the lakes which act as temporary storage areas. By selecting a certain portion of the main channel to compute the *IC channel*, a knickpoint was also observed (Figure 9b). Upstream of its source, the channel network shows a very low sediment connectivity. Linked to location of these storage areas, the catchment-averaged denudation rate is higher than the sub-catchment-averaged denudation rates (Table 3). The spatial division based on IC values between the uppermost and the lower part (Figure 14; Figure 16) correlates with the difference in term of *LMR* and denudation rate in the fluvial catchment (Table 3; Cavalli et al. 2013; Brardinoni et al. 2020). The upper sub-catchments with gentle slopes (shaped by old glacial and present periglacial processes) and affected by erosion processes are characterized by high *LMR*, relatively low sediment connectivity and low denudation rates (long sediment residence times). Whereas the lower part of the catchment seems to have a low *LMR*, it appears to have a relatively high sediment connectivity to the main channel and thus a higher denudation rate than the upper sector (Table 3; Figure 16). In this downstream part, mobilized sediments have a high probability to be transported to the outlet and thus have shorter residence times than in the upstream part. In addition, the presence of a continuous vegetation cover is an indication of less erosion and more stable slopes than upstream. A field investigation would however be required to characterize more objectively and to quantify with accuracy the role of these two sub-catchments on sediment fluxes within this fluvial catchment. Field study could also be useful to visualize and distinguish the type of erosion, transport and deposition processes occurring in the two sectors (Figure 16). Geomorphic structures have a direct influence on the sediment connectivity and denudation rates at catchment scale (Cavalli et al. 2013; Brardinoni et al. 2020).

For the glacial catchment, the link between *LMR*, *IC* maps and catchment-averaged denudation rates are more difficult to interpret. In fact, we only possess one denudation rate measured at the outlet of the *Mins* catchment (Figure 7). Moreover, the pattern of sediment connectivity is homogeneous over the entire area (Figure 13; Figure 14) and the method used does not take into account glacial processes. The *Mins IC* results show a relatively good sediment connectivity to the main channel and the outlet, and especially from the glacier. However, glaciers are temporary sediment storage areas. Glaciers are also a source of sediments mainly produced by abrasion and crushing of larger blocks beneath the glacier (Delaloye et Morard 2019). Therefore, the approach cannot be applied for computing sediment connectivity in the glacial catchment. It is rather adapted to show what would be the state after deglaciation by illustrating potential sediment pathways as a result of rapid climate change, global warming and deglaciation in mountainous environments (de Winter et al. 2012). Global warming cause permafrost degradation, vanishing glaciers and long-term stability reduction of steep or icy mountain slopes (Haeberli et al. 2017). Within the next decades, the ongoing global glacier melting (Houghton et Intergovernmental Panel on Climate Change 1996) will transform these environments into new landscapes of bare bedrock, loose debris, sparse vegetation, lakes and steep slopes with slowly degrading permafrost. In the European Alps, the frequency of large rock avalanches is increasing as a consequence of permafrost warming (Ravanel et Deline 2011; Fischer et al. 2012). Moreover, warm temperatures in permafrost regions may also play a role in the response of slope stability to extreme precipitation events (Rebetez et al. 1997). During the 20th century in all regions of Switzerland, an increase in the number of extreme rainfall events, snowmelt and runoff are observed. These trigger mechanisms contribute to sediment mobilization by hillslope processes, e.g. debris flows events (Rebetez et al. 1997). By the middle of the 21st century, drier conditions in summer and wetter conditions in spring, fall and early winter will likely have a significant impact on the behavior of debris flows in the Swiss Alps. The overall frequency of debris flows events might remain low, but the magnitude might increase due to larger volumes of sediment delivered to the channels (Stoffel et al. 2014).

6. Conclusion

This work allowed to assess the link between of short-term pulses of sediment production by landslides and long-term catchment-averaged denudation rates and to explore possible relations with the structural geomorphic connectivity in two alpine catchments of the upper Rhône Valley. Based on magnitude-frequency distributions, landslide mobilization rates and sediment connectivity indices, links between landslide sediment mobilization rates and denudation rates over thousands of years at catchment scale could be carried out. Our results suggest that the landslide frequency-area distribution is not dependent on the presence of glaciers in catchment and is similar in the glacial *Mins* and the fluvial *Nider* catchment. However, denudation rate is dependent on erosion processes and geomorphic connectivity which are different in the glacial and the fluvial catchment. Indeed, both magnitude-frequency distributions show an inverse-gamma distribution with rollover behavior of small landslides. When disregarding sediment storage and assuming that landslide mobilized material is effectively transported to the outlet, we observe that the *LMR* values are higher in the glacial catchment than in the fluvial one. Moreover, the *LMR* linked to landslides processes (rockfalls and rotational landslides) accounts for a high fraction of catchment-averaged denudation rates in the two catchments of the upper Rhône Valley, and even a higher fraction in the fluvial than in the glacial catchment. This stands in contrast with the catchment-averaged denudation rates that are about ten times higher in the glacial catchment compared to the fluvial.

In the glacial catchment, any clear spatial variation about denudation rate and sediment fluxes across the catchment was highlighted. The *IC* index is more adapted to represent the sediment connectivity in fluvial settings but can be applied in glacial catchments to show the hypothetical state after deglaciation or in the future due to global warming and permafrost degradation. Whereas in the fluvial catchment, the *IC* result divides the catchment into two parts. One the one hand, the upper hanging valley showed a relatively high *LMR* but a low sediment connectivity to the main channel or the outlet and the presence of lakes as sediment storage. Therefore, sediments that are produced in the two upstream sub-catchments have a low probability to be routed to the outlet. The sub-catchments denudation rates are lower than over the entire catchment. On the other hand, the very steep and narrow gorge (in the center of which flows the main channel) presented low *LMR* with high sediment connectivity to its main channel or outlet.

7. References

Aalto, Rolf, Thomas Dunne, et Jean Loup Guyot. (2006). « Geomorphic Controls on Andean Denudation Rates ». *The Journal of Geology* 114 (1): 85-99. https://doi.org/10.1086/498101.

Barboux, Chloé, Reynald Delaloye, et Christophe Lambiel. (2014). « Inventorying Slope Movements in an Alpine Environment Using DInSAR: INVENTORYING OF SLOPE MOVEMENTS IN ALPINE ENVIRONMENT USING DInSAR ». *Earth Surface Processes and Landforms* 39 (15): 2087-99. https://doi.org/10.1002/esp.3603.

Bellin, N., B. van Wesemael, A. Meerkerk, V. Vanacker, et G.G. Barbera. (2009). « Abandonment of Soil and Water Conservation Structures in Mediterranean Ecosystems ». *CATENA* 76 (2): 114-21. https://doi.org/10.1016/j.catena.2008.10.002.

Benda, Lee, et Thomas Dunne. (1997). « Stochastic Forcing of Sediment Supply to Channel Networks from Landsliding and Debris Flow ». *Water Resources Research* 33 (12): 2849-63. https://doi.org/10.1029/97WR02388.

Bennett, G.L., P. Molnar, H. Eisenbeiss, et B.W. McArdell. (2012). « Erosional Power in the Swiss Alps: Characterization of Slope Failure in the Illgraben: EROSIONAL POWER IN THE SWISS ALPS: SLOPE FAILURE IN THE ILLGRABEN ». *Earth Surface Processes and Landforms* 37 (15): 1627-40. https://doi.org/10.1002/esp.3263.

Berger, Catherine, Brian W. McArdell, et Fritz Schlunegger. (2011). « Sediment Transfer Patterns at the Illgraben Catchment, Switzerland: Implications for the Time Scales of Debris Flow Activities ». *Geomorphology* 125 (3): 421-32. https://doi.org/10.1016/j.geomorph.2010.10.019.

Bernard, Thomas G., Dimitri Lague, et Philippe Steer. (2020). « Beyond 2D Inventories : Synoptic 3D Landslide Volume Calculation from Repeat LiDAR Data ». Preprint. Cross-cutting themes: Digital Landscapes: Insights into geomorphological processes from high-resolution topography and quantitative interrogation of topographic data. https://doi.org/10.5194/esurf-2020-73.

Bernet, Matthias, Massimiliano Zattin, John I Garver, Mark T Brandon, et Joseph A Vance. (2001). « Steady-State Exhumation of the European Alps », 4.

Bierman, Paul R., Joanna M. Reuter, Milan Pavich, Allen C. Gellis, Marc W. Caffee, et Jennifer Larsen. (2005). « Using Cosmogenic Nuclides to Contrast Rates of Erosion and Sediment Yield in a Semi-Arid, Arroyo-Dominated Landscape, Rio Puerco Basin, New Mexico ». *Earth Surface Processes and Landforms* 30 (8): 935-53. https://doi.org/10.1002/esp.1255.

Binnie, Steven A., William M. Phillips, Michael A. Summerfield, et L. Keith Fifield. (2007). « Tectonic Uplift, Threshold Hillslopes, and Denudation Rates in a Developing Mountain Range ». *Geology* 35 (8): 743. https://doi.org/10.1130/G23641A.1.

Birkinshaw, S. J., et J. C. Bathurst. (2006). « Model Study of the Relationship between Sediment Yield and River Basin Area ». *Earth Surface Processes and Landforms* 31 (6): 750-61. https://doi.org/10.1002/esp.1291.

Bishop, Paul. (2007). « Long-Term Landscape Evolution: Linking Tectonics and Surface Processes ». *Earth Surface Processes and Landforms* 32 (3): 329-65. https://doi.org/10.1002/esp.1493.

Borselli, Lorenzo, Paola Cassi, et Dino Torri. (2008). « Prolegomena to Sediment and Flow Connectivity in the Landscape: A GIS and Field Numerical Assessment ». *CATENA* 75 (3): 268-77. https://doi.org/10.1016/j.catena.2008.07.006.

Bracken, Louise J., et Jacky Croke. (2007). « The Concept of Hydrological Connectivity and Its Contribution to Understanding Runoff-Dominated Geomorphic Systems ». *Hydrological Processes* 21 (13): 1749-63. https://doi.org/10.1002/hyp.6313.

Bracken, Louise J., Laura Turnbull, John Wainwright, et Patrick Bogaart. (2015). « Sediment Connectivity: A Framework for Understanding Sediment Transfer at Multiple Scales: SEDIMENT CONNECTIVITY: SEDIMENT TRANSFER AT MULTIPLE SCALES ». *Earth Surface Processes and Landforms* 40 (2): 177-88. https://doi.org/10.1002/esp.3635.

Brandolini, Filippo, Emmanuel Reynard, et Manuela Pelfini. (2020). « Multi-Temporal Mapping of the Upper Rhone Valley (Valais, Switzerland): Fluvial Landscape Changes at the End of the Little Ice Age (18th–19th Centuries) ». *Journal of Maps* 16 (2): 212-21. https://doi.org/10.1080/17445647.2020.1724837.

Brardinoni, Francesco, Reto Grischott, Florian Kober, Corrado Morelli, et Marcus Christl. (2020). « Evaluating Debris-flow and Anthropogenic Disturbance on 10Be Concentration in Mountain Drainage Basins: Implications for Functional Connectivity and Denudation Rates across Time Scales » 45: 20.

Broeckx, Jente, Mauro Rossi, Kobe Lijnen, Benjamin Campforts, Jean Poesen, et Matthias Vanmaercke. (2020). « Landslide Mobilization Rates: A Global Analysis and Model ». *Earth-Science Reviews* 201 (février): 102972. https://doi.org/10.1016/j.earscirev.2019.102972.

Broeckx, Jente, Matthias Vanmaercke, Dan Bălteanu, Viorel Chendeş, Mihaela Sima, Petru Enciu, et Jean Poesen. (2016). « Linking Landslide Susceptibility to Sediment Yield at Regional Scale: Application to Romania ». *Geomorphology* 268 (septembre): 222-32. https://doi.org/10.1016/j.geomorph.2016.06.012.

Brown, Anthony G., Christopher Carey, Gilles Erkens, Markus Fuchs, Thomas Hoffmann, Jean-Jacques Macaire, Klaus-Martin Moldenhauer, et Des E. Walling. (2009). « From Sedimentary Records to Sediment Budgets: Multiple Approaches to Catchment Sediment Flux ». *Geomorphology* 108 (1-2): 35-47. https://doi.org/10.1016/j.geomorph.2008.01.021.

Burbank, Douglas West, et Robert S. Anderson. (2012). *Tectonic geomorphology*. 2nd ed. Chichester, West Sussex ; Hoboken, N.J: J. Wiley & Sons.

Burbank, Douglas West, Robert S Anderson, et Robert S Anderson. (2012). *Tectonic Geomorphology*. Chichester, West Sussex; Hoboken, NJ: J. Wiley & Sons.

Cavalli, M., et L. Marchi. (2008). « Characterisation of the Surface Morphology of an Alpine Alluvial Fan Using Airborne LiDAR ». *Natural Hazards and Earth System Sciences* 8 (2): 323-33. https://doi.org/10.5194/nhess-8-323-2008.

Cavalli, Marco, Sebastiano Trevisani, Francesco Comiti, et Lorenzo Marchi. (2013). « Geomorphometric Assessment of Spatial Sediment Connectivity in Small Alpine Catchments ». *Geomorphology* 188 (avril): 31-41. https://doi.org/10.1016/j.geomorph.2012.05.007.

Clapuyt, François, Veerle Vanacker, Marcus Christl, Kristof Van Oost, et Fritz Schlunegger. (2019). « Spatio-Temporal Dynamics of Sediment Transfer Systems in Landslide-Prone Alpine Catchments ». *Solid Earth*, 16.

Clapuyt, François, Veerle Vanacker, Fritz Schlunegger, et Kristof Van Oost. (2017). « Unravelling Earth Flow Dynamics with 3-D Time Series Derived from UAV-SfM Models ». *Earth Surface Dynamics* 5 (4): 791-806. https://doi.org/10.5194/esurf-5-791-2017.

Clauset, Aaron, Cosma Rohilla Shalizi, et M. E. J. Newman. (2009). « Power-Law Distributions in Empirical Data ». *SIAM Review* 51 (4): 661-703. https://doi.org/10.1137/070710111.

Clubb, Fiona J., Simon M. Mudd, David T. Milodowski, Stuart W.D. Grieve, et Martin D. Hurst. (2017). *Lsdchannelextraction V 1.0*. Zenodo. https://doi.org/10.5281/ZENODO.824198.

Cook, Kristen L., Jens M. Turowski, et Niels Hovius. (2020). « Width Control on Event-scale Deposition and Evacuation of Sediment in Bedrock-confined Channels ». *Earth Surface Processes and Landforms* 45 (14): 3702-13. https://doi.org/10.1002/esp.4993.

Cooper, James R., John Wainwright, Anthony J. Parsons, Yuichi Onda, Tomomi Fukuwara, Eiichiro Obana, Ben Kitchener, Edward J. Long, et Graham H. Hargrave. (2012). « A New Approach for Simulating the Redistribution of Soil Particles by Water Erosion: A Marker-in-Cell Model: SOIL EROSION, MARKER-IN-CELL MODEL ». *Journal of Geophysical Research: Earth Surface* 117 (F4): n/a-n/a. https://doi.org/10.1029/2012JF002499.

Crema, Stefano, et Marco Cavalli. (2018). « SedInConnect: A Stand-Alone, Free and Open Source Tool for the Assessment of Sediment Connectivity ». *Computers & Geosciences* 111 (février): 39-45. https://doi.org/10.1016/j.cageo.2017.10.009.

Crozier, M.J., et T. Glade. (1999). « Frequency and Magnitude of Landsliding: Fundamental Research Issues ». *Zeitschrift Für Geomorphologie Supplement Volumes* 115 (juillet): 141-55. https://doi.org/10.1127/zfgsuppl/115/1999/141.

Delaloye, R., et Sébastien Morard. (2019). « Géomorphologie périglaciaire ». Géographie Dép. Géosciences, Université de Fribourg - GG.02262-263.

Dunai, Tibor J. (2000). « Scaling Factors for Production Rates of in Situ Produced Cosmogenic Nuclides: A Critical Reevaluation ». *Earth and Planetary Science Letters* 176 (1): 157-69. https://doi.org/10.1016/S0012-821X(99)00310-6.

Egholm, David L., Mads F. Knudsen, et Mike Sandiford. (2013). « Lifespan of Mountain Ranges Scaled by Feedbacks between Landsliding and Erosion by Rivers ». *Nature* 498 (7455): 475-78. https://doi.org/10.1038/nature12218.

Federal Office of Topography swisstopo. s. d. « Geodata and Applications ». Federal Office of Topography Swisstopo. Consulté le 6 mai 2021a. https://www.swisstopo.admin.ch/en/geodata.html.

———. s. d. « Swiss Geoportal ». geo.admin.ch. Consulté le 6 mai 2021b. https://map.geo.admin.ch.

Fischer, L., R. S. Purves, C. Huggel, J. Noetzli, et W. Haeberli. (2012). « On the Influence of Topographic, Geological and Cryospheric Factors on Rock Avalanches and Rockfalls in High-Mountain Areas ». *Natural Hazards and Earth System Sciences* 12 (1): 241-54. https://doi.org/10.5194/nhess-12-241-2012.

Fryirs, Kirstie. (2013). « (Dis)Connectivity in Catchment Sediment Cascades: A Fresh Look at the Sediment Delivery Problem: (DIS)CONNECTIVITY IN CATCHMENT SEDIMENT CASCADES ». *Earth Surface Processes and Landforms* 38 (1): 30-46. https://doi.org/10.1002/esp.3242.

Fuller, Christopher W., Sean D. Willett, Niels Hovius, et Rudy Slingerland. (2003). « Erosion Rates for Taiwan Mountain Basins: New Determinations from Suspended Sediment Records and a Stochastic Model of Their Temporal Variation ». *The Journal of Geology* 111 (1): 71-87. https://doi.org/10.1086/344665.

Gabet, Emmanuel J., et Simon M. Mudd. (2009). « A Theoretical Model Coupling Chemical Weathering Rates with Denudation Rates ». *Geology* 37 (2): 151-54. https://doi.org/10.1130/G25270A.1.

Galli, Mirco, Francesca Ardizzone, Mauro Cardinali, Fausto Guzzetti, et Paola Reichenbach. (2008). « Comparing Landslide Inventory Maps ». *Geomorphology* 94 (3-4): 268-89. https://doi.org/10.1016/j.geomorph.2006.09.023.

Granger, DE, et CS Riebe. (2003). « Cosmogenic Nuclides in Weathering and Erosion. » *Holland HD, Turekian KK, eds. Treatise on Geochemistry.* 5 (First Edit).

Guns, Marie, et Veerle Vanacker. (2014). « Shifts in Landslide Frequency–Area Distribution after Forest Conversion in the Tropical Andes ». *Anthropocene* 6 (juin): 75-85. https://doi.org/10.1016/j.ancene.2014.08.001.

Guzzetti, Fausto, Francesca Ardizzone, Mauro Cardinali, Mauro Rossi, et Daniela Valigi. (2009). « Landslide Volumes and Landslide Mobilization Rates in Umbria, Central Italy ». *Earth and Planetary Science Letters* 279 (3-4): 222-29. https://doi.org/10.1016/j.epsl.2009.01.005.

Guzzetti, Fausto, Bruce D Malamud, Donald L Turcotte, et Paola Reichenbach. (2002). « Power-Law Correlations of Landslide Areas in Central Italy ». *Earth and Planetary Science Letters* 195 (3-4): 169-83. https://doi.org/10.1016/S0012-821X(01)00589-1.

Guzzetti, Fausto, Alessandro Cesare Mondini, Mauro Cardinali, Federica Fiorucci, Michele Santangelo, et Kang-Tsung Chang. (2012). « Landslide Inventory Maps: New Tools for an Old Problem ». *Earth-Science Reviews* 112 (1-2): 42-66. https://doi.org/10.1016/j.earscirev.2012.02.001.

Guzzetti, Fausto, Paola Reichenbach, Mauro Cardinali, Mirco Galli, et Francesca Ardizzone. (2005). « Probabilistic Landslide Hazard Assessment at the Basin Scale ». *Geomorphology* 72 (1-4): 272-99. https://doi.org/10.1016/j.geomorph.2005.06.002.

Hack, John T. (1975). « Dynamic equilibrium and landscape evolution ». In *Theories of landform development*, 1:87-102.

Haeberli, Wilfried, Yvonne Schaub, et Christian Huggel. (2017). « Increasing Risks Related to Landslides from Degrading Permafrost into New Lakes in De-Glaciating Mountain Ranges ». *Geomorphology* 293 (septembre): 405-17. https://doi.org/10.1016/j.geomorph.2016.02.009.

Hooke, Janet. (2003). « Coarse Sediment Connectivity in River Channel Systems: A Conceptual Framework and Methodology ». *Geomorphology* 56 (1-2): 79-94. https://doi.org/10.1016/S0169-555X(03)00047-3.

Houghton, John Theodore, et Intergovernmental Panel on Climate Change, éd. (1996). *Climate change 1995: the science of climate change*. Cambridge ; New York: Cambridge University Press.

Hovius, Niels, Colin P Stark, et Philip A Allen. (1997). « Geology: Sediment Flux from a Mountain Belt Derived by Landslide Mapping », 5.

Hovius, Niels, Colin P. Stark, Chu Hao-Tsu, et Lin Jiun-Chuan. (2000). « Supply and Removal of Sediment in a Landslide-Dominated Mountain Belt: Central Range, Taiwan ». *The Journal of Geology* 108 (1): 73-89. https://doi.org/10.1086/314387.

Hungr, Oldrich, Serge Leroueil, et Luciano Picarelli. (2014). « The Varnes Classification of Landslide Types, an Update ». *Landslides* 11 (2): 167-94. https://doi.org/10.1007/s10346-013-0436-y.

Ivy-Ochs, Susan, et Florian Kober. (2008). « Surface Exposure Dating with Cosmogenic Nuclides ». *E&G Quaternary Science Journal* 57 (1/2): 179-209. https://doi.org/10.3285/eg.57.1-2.7.

Katz, O, et E Aharonov. (2006). « Landslides in Vibrating Sand Box: What Controls Types of Slope Failure and Frequency Magnitude Relations? » *Earth and Planetary Science Letters* 247 (3-4): 280-94. https://doi.org/10.1016/j.epsl.2006.05.009.

Kelly, Meredith A., Jean-François Buoncristiani, et Christian Schlüchter. (2004). « A Reconstruction of the Last Glacial Maximum (LGM) Ice-Surface Geometry in the Western Swiss Alps and Contiguous Alpine Regions in Italy and France ». *Eclogae Geologicae Helvetiae* 97 (1): 57-75. https://doi.org/10.1007/s00015-004-1109-6.

Kenner, R., Y. Bühler, R. Delaloye, C. Ginzler, et M. Phillips. (2014). « Monitoring of High Alpine Mass Movements Combining Laser Scanning with Digital Airborne Photogrammetry ». *Geomorphology* 206 (février): 492-504. https://doi.org/10.1016/j.geomorph.2013.10.020.

Kenner, Robert. (2018). « Monitoring Mass Movements Using Georeferenced Time-Lapse Photography_ Ritigraben Rock Glacier, Western Swiss Alps ». *Cold Regions Science and Technology*, 8.

Korup, Oliver, Alexander L. Densmore, et Fritz Schlunegger. (2010). « The Role of Landslides in Mountain Range Evolution ». *Geomorphology* 120 (1-2): 77-90. https://doi.org/10.1016/j.geomorph.2009.09.017.

Kummert, Mario, et Reynald Delaloye. (2018). « Mapping and Quantifying Sediment Transfer between the Front of Rapidly Moving Rock Glaciers and Torrential Gullies ». *Geomorphology* 309 (mai): 60-76. https://doi.org/10.1016/j.geomorph.2018.02.021.

Kummert, Mario, Reynald Delaloye, et Luc Braillard. (2018). « Erosion and Sediment Transfer Processes at the Front of Rapidly Moving Rock Glaciers: Systematic Observations with Automatic Cameras in the Western Swiss Alps ». *Permafrost and Periglacial Processes* 29 (1): 21-33. https://doi.org/10.1002/ppp.1960.

Labhart, TP. (1977). « Aarmassiv und Gotthardmassiv. » *Samllung Geolischer Fuehrer 63*, 173.
Larsen, Isaac J., David R. Montgomery, et Harvey M. Greenberg. (2014). « The Contribution of Mountains to Global Denudation ». *Geology* 42 (6): 527-30. https://doi.org/10.1130/G35136.1.

Larsen, Isaac J., David R. Montgomery, et Oliver Korup. (2010). « Landslide Erosion Controlled by Hillslope Material ». *Nature Geoscience* 3 (4): 247-51. https://doi.org/10.1038/ngeo776.

Larsen, Isaac J., David R. Montgomery, et Harvey M. Greenberg. (2014). « The Contribution of Mountains to Global Denudation ». *Geology* 42 (6): 527-30. https://doi.org/10.1130/G35136.1.

Lugon, Ralph. (2010). « Rock-Glacier Dynamics and Magnitude–Frequency Relations of Debris Flows in a High-Elevation Watershed: Ritigraben, Swiss Alps ». *Global and Planetary Change*, 9.

Malamud, Bruce D, Donald L Turcotte, Fausto Guzzetti, et Paola Reichenbach. (2004). « Landslide Inventories and Their Statistical Properties », 25.

Marc, O., N. Hovius, P. Meunier, T. Uchida, et S. Hayashi. (2015). « Transient Changes of Landslide Rates after Earthquakes ». *Geology* 43 (10): 883-86. https://doi.org/10.1130/G36961.1.

Massonnet, Didier, et Kurt L. Feigl. (1998). « Radar Interferometry and Its Application to Changes in the Earth's Surface ». *Reviews of Geophysics* 36 (4): 441-500. https://doi.org/10.1029/97RG03139.

Mey, Jürgen, Dirk Scherler, Andrew D. Wickert, David L. Egholm, Magdala Tesauro, Taylor F. Schildgen, et Manfred R. Strecker. (2016). « Glacial Isostatic Uplift of the European Alps ». *Nature Communications* 7 (1): 13382. https://doi.org/10.1038/ncomms13382.

Mitasova, Helena, Jaroslav Hofierka, Maros Zlocha, et Louis R. Iverson. (1996). « Modelling Topographic Potential for Erosion and Deposition Using GIS ». *International Journal of Geographical Information Systems* 10 (5): 629-41. https://doi.org/10.1080/02693799608902101.

Norton, Kevin P., Friedhelm von Blanckenburg, Roman DiBiase, Fritz Schlunegger, et

Peter W. Kubik. (2011). « Cosmogenic 10Be-Derived Denudation Rates of the Eastern and Southern European Alps ». *International Journal of Earth Sciences* 100 (5): 1163-79. https://doi.org/10.1007/s00531-010-0626-y.

Norton, Kevin P., Friedhelm von Blanckenburg, et Peter W. Kubik. (2010). « Cosmogenic Nuclide-Derived Rates of Diffusive and Episodic Erosion in the Glacially Sculpted Upper Rhone Valley, Swiss Alps ». *Earth Surface Processes and Landforms*, n/a-n/a. https://doi.org/10.1002/esp.1961.

Olivier, Jean-Michel, Marie-José Dole-Olivier, Claude Amoros, Georges Carrel, Florian Malard, Nicolas Lamouroux, et Jean-Paul Bravard. (2009). « The Rhône River Basin ». In *Rivers of Europe*, 247-95. Elsevier. https://doi.org/10.1016/B978-0-12-369449-2.00007-2.

Parker, R. N., G. T. Hancox, D. N. Petley, C. I. Massey, A. L. Densmore, et N. J. Rosser. (2015). « Spatial Distributions of Earthquake-Induced Landslides and Hillslope Preconditioning in the Northwest South Island, New Zealand ». *Earth Surface Dynamics* 3 (4): 501-25. https://doi.org/10.5194/esurf-3-501-2015.

Passalacqua, Paola, Patrick Belmont, Dennis M. Staley, Jeffrey D. Simley, J Ramon Arrowsmith, Collin A. Bode, Christopher Crosby, et al. (2015). « Analyzing High Resolution Topography for Advancing the Understanding of Mass and Energy Transfer through Landscapes: A Review ». *Earth-Science Reviews* 148 (septembre): 174-93. https://doi.org/10.1016/j.earscirev.2015.05.012.

Peizhen, Zhang, Peter Molnar, et William R Downs. (2001). « Increased Sedimentation Rates and Grain Sizes 2±4 Myr Ago Due to the Influence of Climate Change on Erosion Rates » 410: 7.

Pelletier, Jon D., et Tyson L. Swetnam. (2017). « Asymmetry of Weathering-Limited Hillslopes: The Importance of Diurnal Covariation in Solar Insolation and Temperature: Asymmetry of Weathering-Limited Hillslopes ». *Earth Surface Processes and Landforms* 42 (9): 1408-18. https://doi.org/10.1002/esp.4136.

Ravanel, Ludovic, et Philip Deline. (2011). « Climate Influence on Rockfalls in High-Alpine Steep Rockwalls: The North Side of the Aiguilles de Chamonix (Mont Blanc Massif) since the End of the 'Little Ice Age' ». *The Holocene* 21 (2): 357-65. https://doi.org/10.1177/0959683610374887.

Rebetez, Martine, Ralph Lugon, et Pierre-Alain Baeriswyl. (1997). « Climatic Change and Debris Flows in High Mountain Regions: The Case Study of the Ritigraben Torrent (Swiss Alps) ». In *Climatic Change at High Elevation Sites*, édité par Henry F. Diaz, Martin Beniston, et Raymond S. Bradley, 139-57. Dordrecht: Springer Netherlands. https://doi.org/10.1007/978-94-015-8905-5_8.

Renard, K. G., USA, et USA, éd. (1997). *Predicting Soil Erosion by Water: A Guide to Conservation Planning with the Revised Universal Soil Loss Equation (RUSLE)*. Agriculture Handbook 703. Washington, D. C.

Reynard, Emmanuel. (2009). « Les sources cartographiques pour l'histoire du Rhône valaisan », 17.

Rickenmann, Dieter. (2005). « Runout Prediction Methods ». In *Debris-Flow Hazards and Related Phenomena*, 305-24. Springer Praxis Books. Berlin, Heidelberg: Springer Berlin Heidelberg. https://doi.org/10.1007/3-540-27129-5_13.

Roe, G. H., K. X. Whipple, et J. K. Fletcher. (2008). « Feedbacks among Climate, Erosion, and Tectonics in a Critical Wedge Orogen ». *American Journal of Science* 308 (7): 815-42. https://doi.org/10.2475/07.2008.01.

Roering, Joshua J., James W. Kirchner, et William E. Dietrich. (2001). « Hillslope Evolution by Nonlinear, Slope-Dependent Transport: Steady State Morphology and Equilibrium Adjustment Timescales ». *Journal of Geophysical Research: Solid Earth* 106 (B8): 16499-513. https://doi.org/10.1029/2001JB000323.

Schlatter, Andreas, Dieter Schneider, Alain Geiger, et Hans-Gert Kahle. (2005). « Recent Vertical Movements from Precise Levelling in the Vicinity of the City of Basel, Switzerland ». *International Journal of Earth Sciences* 94 (4): 507-14. https://doi.org/10.1007/s00531-004-0449-9.

Schlögel, R., J.-P. Malet, P. Reichenbach, A. Remaître, et C. Doubre. (2015). « Analysis of a Landslide Multi-Date Inventory in a Complex Mountain Landscape: The Ubaye Valley Case Study ». *Natural Hazards and Earth System Sciences* 15 (10): 2369-89. https://doi.org/10.5194/nhess-15-2369-2015.

Schoch, Anna, Jan Henrik Blöthe, Thomas Hoffmann, et Lothar Schrott. (2018). « Multivariate Geostatistical Modeling of the Spatial Sediment Distribution in a Large Scale Drainage Basin, Upper Rhone, Switzerland ». *Geomorphology* 303 (février): 375-92. https://doi.org/10.1016/j.geomorph.2017.11.026.

Stanley, Steven M., et John A. Luczaj. (2015). *Earth system history: Steven M. Stanley, University of Hawaii, John A. Luczaj, University of Wisconsin - Green Bay*. Fourth edition. New York, NY: W.H. Freeman and Company, a Macmillan Higher Education company.

Stark, C. P., et F. Guzzetti. (2009). « Landslide Rupture and the Probability Distribution of Mobilized Debris Volumes ». *Journal of Geophysical Research* 114 (juin): F00A02. https://doi.org/10.1029/2008JF001008.

Stark, Colin P., et Niels Hovius. (2001). « The Characterization of Landslide Size

Distributions ». *Geophysical Research Letters* 28 (6): 1091-94. https://doi.org/10.1029/2000GL008527.

Stoffel, Markus, Thomas Mendlik, Michelle Schneuwly-Bollschweiler, et Andreas Gobiet. (2014). « Possible Impacts of Climate Change on Debris-Flow Activity in the Swiss Alps ». *Climatic Change* 122 (1-2): 141-55. https://doi.org/10.1007/s10584-013-0993-z.

Strozzi, Tazio, Reynald Delaloye, Andreas Kääb, Christian Ambrosi, Eric Perruchoud, et Urs Wegmüller. (2010). « Combined Observations of Rock Mass Movements Using Satellite SAR Interferometry, Differential GPS, Airborne Digital Photogrammetry, and Airborne Photography Interpretation ». *Journal of Geophysical Research* 115 (F1): F01014. https://doi.org/10.1029/2009JF001311.

Stüwe, Kurt, et Terence D. Barr. (1998). « On Uplift and Exhumation during Convergence ». *Tectonics* 17 (1): 80-88. https://doi.org/10.1029/97TC02557.

Tanyaş, Hakan, Kate E. Allstadt, et Cees J. van Westen. (2018). « An Updated Method for Estimating Landslide-Event Magnitude: An Updated Method for Estimating Landslide-Event Magnitude ». *Earth Surface Processes and Landforms* 43 (9): 1836-47. https://doi.org/10.1002/esp.4359.

Tanyaş, Hakan, Cees J. Westen, Kate E. Allstadt, et Randall W. Jibson. (2019). « Factors Controlling Landslide Frequency–Area Distributions ». *Earth Surface Processes and Landforms* 44 (4): 900-917. https://doi.org/10.1002/esp.4543.

Tanyaş, Hakan, Cees J. van Westen, Kate E. Allstadt, M. Anna Nowicki Jessee, Tolga Görüm, Randall W. Jibson, Jonathan W. Godt, et al. (2017). « Presentation and Analysis of a Worldwide Database of Earthquake-Induced Landslide Inventories: Earthquake-Induced Landslide Inventories ». *Journal of Geophysical Research: Earth Surface* 122 (10): 1991-2015. https://doi.org/10.1002/2017JF004236.

Tarboton, David G. (1997). « A New Method for the Determination of Flow Directions and Upslope Areas in Grid Digital Elevation Models ». *Water Resources Research* 33 (2): 309-19. https://doi.org/10.1029/96WR03137.

Tchalenko, J. S.; Morgenstern, N. R. (1967). « Microscopic Structures in Kaolin Subjected to Direct Shear ». https://doi.org/10.7939/R3TB0XZ0G.

Trevisani, S., M. Cavalli, et L. Marchi. (2010). « Reading the Bed Morphology of a Mountain Stream: A Geomorphometric Study on High-Resolution Topographic Data ». *Hydrology and Earth System Sciences* 14 (2): 393-405. https://doi.org/10.5194/hess-14-393-2010.

Turner, A. Keith, et Robert L. Schuster, éd. (1996). *Landslides: investigation and* *mitigation*. Special report / Transportation Research Board, National Research Council 247. Washington, D.C: National Academy Press.

Turowski, Jens M., et Kristen L. Cook. (2017). « Field Techniques for Measuring Bedrock Erosion and Denudation: Field Techniques for Measuring Bedrock Erosion and Denudation ». *Earth Surface Processes and Landforms* 42 (1): 109-27. https://doi.org/10.1002/esp.4007.

Ustaszewski, Michaela, et O. Adrian Pfiffner. (2008). « Neotectonic Faulting, Uplift and Seismicity in the Central and Western Swiss Alps ». *Geological Society, London, Special Publications* 298 (1): 231-49. https://doi.org/10.1144/SP298.12.

Van Den Eeckhaut, M., J. Poesen, G. Govers, G. Verstraeten, et A. Demoulin. (2007). « Characteristics of the Size Distribution of Recent and Historical Landslides in a Populated Hilly Region ». *Earth and Planetary Science Letters* 256 (3-4): 588-603. https://doi.org/10.1016/j.epsl.2007.01.040.

Vanacker, V., F. von Blanckenburg, T. Hewawasam, et P.W. Kubik. (2007). « Constraining Landscape Development of the Sri Lankan Escarpment with Cosmogenic Nuclides in River Sediment ». *Earth and Planetary Science Letters* 253 (3-4): 402-14. https://doi.org/10.1016/j.epsl.2006.11.003.

Vanacker, Veerle, Friedhelm von Blanckenburg, Gerard Govers, Armando Molina, Benjamin Campforts, et Peter W. Kubik. (2015). « Transient River Response, Captured by Channel Steepness and Its Concavity ». *Geomorphology* 228 (janvier): 234-43. https://doi.org/10.1016/j.geomorph.2014.09.013.

Vanacker, Veerle, Friedhelm von Blanckenburg, Gerard Govers, Armando Molina, Jean Poesen, Jozef Deckers, et Peter Kubik. (2007). « Restoring Dense Vegetation Can Slow Mountain Erosion to near Natural Benchmark Levels ». *Geology* 35 (4): 303. https://doi.org/10.1130/G23109A.1.

Vanacker, Veerle, Marie Guns, Francois Clapuyt, Vincent Balthazar, Gustavo Tenorio, et Armando Molina. (2020). « Spatio-Temporal Patterns of Landslides and Erosion in Tropical Andean Catchments ». *Pirineos* 75 (septembre): 051. https://doi.org/10.3989/pirineos.2020.175001.

Vanmaercke, Matthias, Jean Poesen, Gert Verstraeten, Joris de Vente, et Faruk Ocakoglu. (2011). « Sediment Yield in Europe: Spatial Patterns and Scale Dependency ». *Geomorphology* 130 (3-4): 142-61. https://doi.org/10.1016/j.geomorph.2011.03.010.

Varnes, David J. (1978). « Slope Movement Types and Processes. » *Transp Res Board Spec Rep.*, Special report: Landslides: Analysis and Control, Transportation Research Board,Washington, D.C., 176 (11-33).

Whipple, Kelin X., et Gregory E. Tucker. (1999). « Dynamics of the Stream-Power River Incision Model: Implications for Height Limits of Mountain Ranges, Landscape Response Timescales, and Research Needs ». *Journal of Geophysical Research: Solid Earth* 104 (B8): 17661-74. https://doi.org/10.1029/1999JB900120.

Winter, Ilja L. de, Joep E.A. Storms, et Irina Overeem. (2012). « Numerical Modeling of Glacial Sediment Production and Transport during Deglaciation ». *Geomorphology* 167-168 (septembre): 102-14. https://doi.org/10.1016/j.geomorph.2012.05.023.

Wischmeier, W.H., et D.D. Smith. (1978). « Predicting rainfall erosion losses ». In *A guide to conservation planning.*, 537:58. U.S. Department of Agriculture.

8. List of figures

Figure 1 : Rock-surface erosion and cosmogenic concentrations (Burbank et Anderson, 2012). 7

Figure 2 : Schematic of the main components of the non-cumulative from Tanyas et al. (2019). 11

Figure 3: IC channels map computed with reference to: a) the outlet of the studied catchments and b) the main channels and lakes from Cavalli et al. (2013). 13

Figure 4: Methodological workflow applied in this study. 14

Figure 5 : Location map of the upper Rhône Valley, showing the canton of Valais with the two catchments Mins and Nider. 16

Figure 6 : Connectivity index upslope and downslope components (modified by Cavalli et al., 2013 after Borselli et al., 2008). 20

Figure 7 : Channel networks (computed with the SAGA QGIS Module “Channel network”; threshold value greater than 50 000 m^2), main channels and selected main channels used for the IC index for the Mins catchment of the upper Rhône Valley. Background map : https://www.swisstopo.admin.ch/en/geodata.html. 22

Figure 8 : Channel networks (computed with the SAGA QGIS Module ”Channel network”; threshold value greater than 50 000 m^2), main channels and selected main channels used for the IC index for the Nider catchment of the upper Rhône Valley. Background map : https://www.swisstopo.admin.ch/en/geodata.html. 22

Figure 9 : Longitudinal profile and $f(A^mS^n)$ (with a moving average window of 40 m) of: a) Mins (Figure 7) and b) Nider main channel (Figure 8). 23

Figure 10 : The landslide inventory map for two tributary catchments located in the upper Rhône Valley, Swiss Alps. This map was produced based on orthophotos, digital elevation models and satellite image interpretation. This figure’s location is shown in Figure 5. 25

Figure 11: Landslide probability density $p(AL)$ (Equation 5) as a function of landslide area AL for: a) Mins and b) Nider landslide inventory on logarithmic axes. The red line is the best 3-parameter inverse-gamma fit (Equation 1) of this distribution by maximum likelihood optimization with parameter values: (a) $\rho = 0.29 \pm 0.05$, $a = 15.38 \pm 3.21$, $s = 0.97 \pm 1.17$ (RSE: 0.0010 on 37 degrees of freedom) for Nider and (b) $\rho = 0.18 \pm 0.03$, $a = 5.75 \pm 1.42$, $s = 3.26 \pm 0.53$ (RSE: 0.0014 on 30 degrees of freedom) for Mins. ... 27

Figure 12 : Distribution of IC values per catchment: a) Mins IC outlet, b) Nider IC outlet, c) Mins IC channel and d) Nider IC channel. 30

Figure 13 : IC outlet as an index of connectivity computed with reference to the outlet of the studied catchments. IC values are classified by equal interval. 31

Figure 14 : IC channel as an index of connectivity computed with reference to the main channel of the studied catchments. IC values are classified by equal interval. 31

Figure 15 : Catchment-averaged denudation rates of fluvial (in green) and glacial (in blue) catchments of the upper Rhône Valley (Norton et al. 2010). Location of the selected catchments are shown in Appendix 3. 38

Figure 16 : Division of the Nider catchment into two sectors according to the values of the LMRs and IC. 40

9. List of tables

Table 1 : Input raster and shapefile files used in the SedInConnect application to compute IC index with respect to the main outlet (IC outlet) and with respect to the main channel (IC channel) for each alpine catchment Mins and Nider. 21

Table 2 : Three-parameter inverse-gamma fitting of the landslide area distributions of the inventory (Equation 1) 26

Table 3 : Denudation rate (Norton et al. 2010), estimated TVL (Equation 3) and LMR (Equation 4) for (sub)-catchments. High and low LMR are respectively related to an inventory time span of 40 yr and 100 yr. 28

Table 4 : Main statistics of the sediment connectivity index with respect to outlets (IC outlet) and main channel (IC channel) of the two study catchments.. 29

Table 5: Power law exponents of different inventories published in the literature. 34

10. Appendix

Appendix 1 : Total number of landslides per landslide type per bin as a function of landslide area in the: a) Mins and b) Nider catchments. Values on x and y axes are shown on a logarithmic scale.

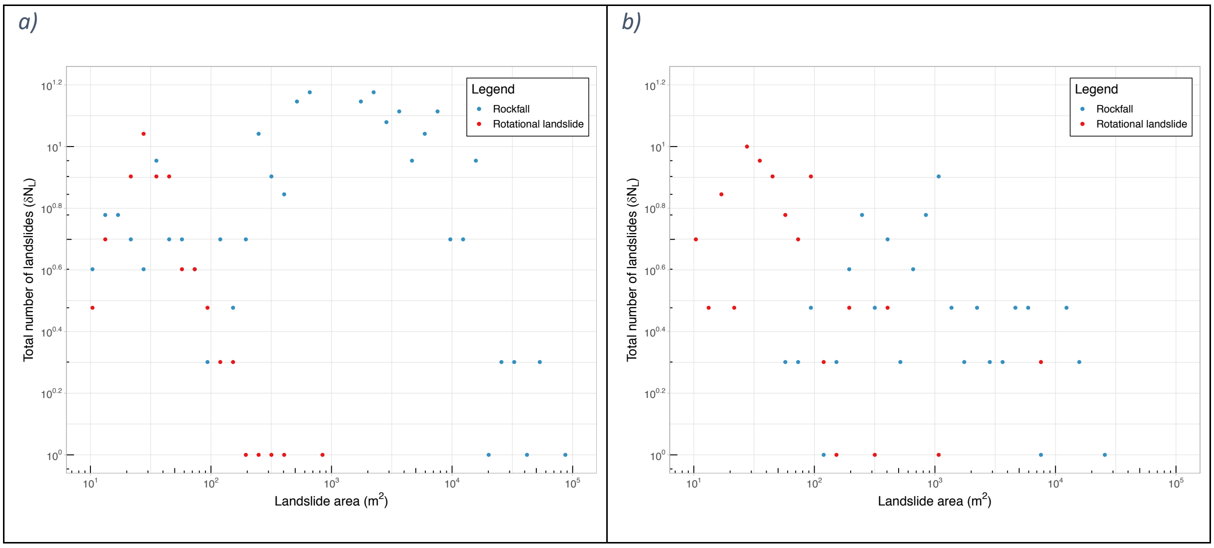

Appendix 2 : Non-cumulative (in black) and cumulative (in red) number of landslides (rockfalls and rotational landslides combined) per bin for: a) Mins and b) Nider catchments. Values on x and y axes are shown on a logarithmic scale.

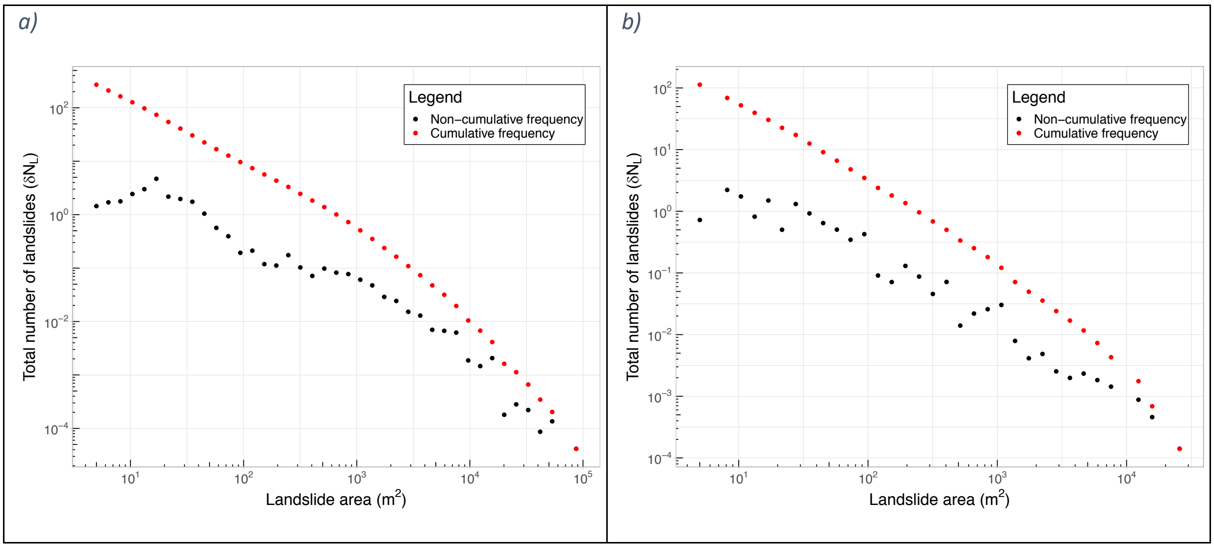

Appendix 3 : Location map of the 13 tributaries where long-term catchment-averaged denudation rates are quantified. (Glacial catchment indicated by squares, fluvial catchment by diamonds and southern catchment by triangles). Soil sample locations are represented by the white symbols: ridge top with a diamond, valley side with a star, triangular faceted surface with a triangle. (from Norton et al., 2010).

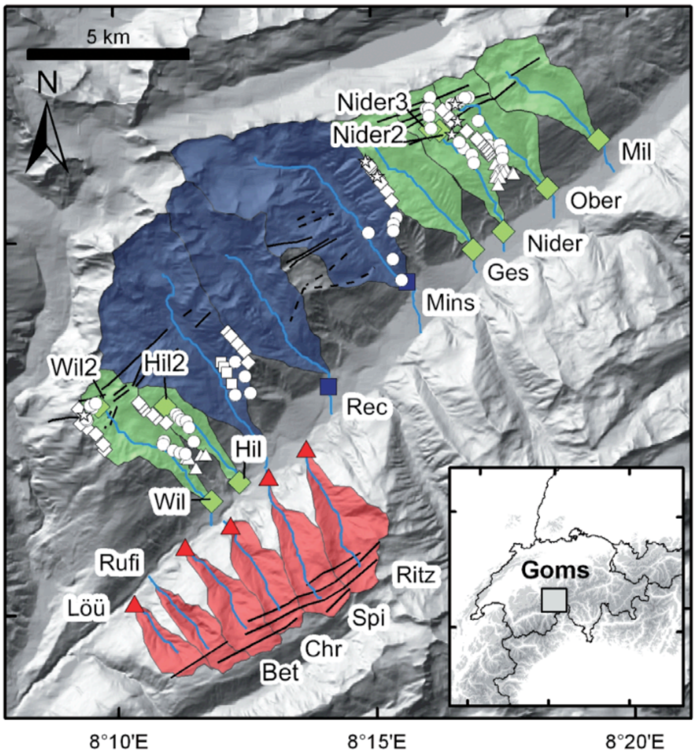

Appendix 4 : Segmentation of the Strimm catchment (Italian Eastern Alps) into three sectors according to IC values (from Cavalli et al. 2013)

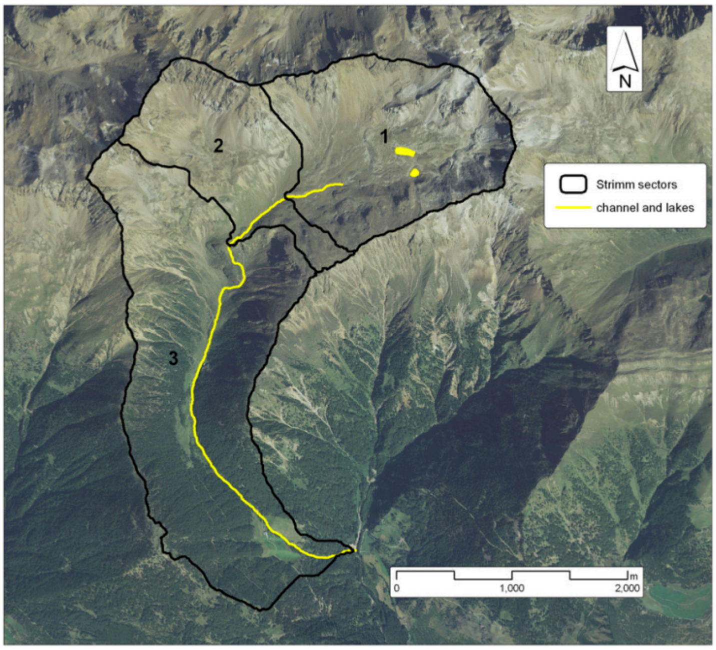

Biographie de l'auteur

Coordonnées

Bayens Mathilde
Adresse : Rue Grégoire Jurion 40, 7120 Vellereille-les-Brayeux
Téléphone : 0493/70.64.85
bayensmathilde@icloud.com

Parcours scolaire

2010 - 2016: Collège Notre Dame de Bonne-Espérance (Estinnes) (obtention du CESS, option latin-math)
Janvier - mars 2016: Programme EXPEDIS-High school WEP en Afrique du Sud (Cape Town)
2016 - 2019: Bachelier en Sciences géographiques à l'UCLouvain – avec distinction
2019 - 2021: Master en Sciences géographiques à l'UCLouvain (orientation générale à finalité approfondie)
Février - juillet 2020: Programme Erasmus à l'Université de Fribourg (CH)

UNIVERSITÉ CATHOLIQUE DE LOUVAIN
Faculté des sciences
Place des sciences, 2 bte L6.06.01, 1348 Louvain-la-Neuve, Belgique | **www.uclouvain.be/sc**